inorganics

MDPI

Review

In Situ Techniques for Characterization of Layered Double Hydroxide-Based Oxygen Evolution Catalysts

Andraž Mavrič * and Matjaž Valant

Materials Research Laboratory, University of Nova Gorica, 5000 Nova Gorica, Slovenia; matjaz.valant@ung.si
* Correspondence: andraz.mavric@ung.si

Abstract: Functional layered double hydroxide (LDH) usually contains different cationic substitutes to increase the activity of the oxygen evolution reaction (OER). The intrinsic OER activity of LDH materials is connected with the chemical composition and dispersion of metal cations substitutions in the matrix phase. The potential induced phase transitions, in particular hydroxide-to-oxyhydroxide transitions, are a predisposition for the high OER activity of LDH materials and can be followed by coupling the electrochemical experiments with spectroscopic techniques. The understanding of LDH catalysts under electrochemical conditions also allows an understanding of the behavior of OER catalysts based on transition metals, metal-chalcogenides, -pnictides, -carbides, and metal–organic frameworks. The surfaces of those materials are intrinsically poor OER catalysts. However, they act as precursors to catalysts, which are oxidized into a metal (oxy)hydroxide. This review summarizes the use of in situ techniques for the characterization of LDH-based OER electrocatalysts and presents the influence of these techniques on the understanding of potential induced phase transitions, identification of active sites, and reaction mechanisms.

Keywords: oxygen evolution reaction; layered double hydroxide; in-situ characterization

check for updates

Citation: Mavrič, A.; Valant, M. In Situ Techniques for Characterization of Layered Double Hydroxide-Based Oxygen Evolution Catalysts. *Inorganics* **2023**, *11*, 296. https://doi.org/10.3390/inorganics11070296

Academic Editors: Haihua Xu, Sadaf Mutahir and Sidi Zhu

Received: 30 May 2023
Revised: 22 June 2023
Accepted: 25 June 2023
Published: 13 July 2023

1. Introduction

To understand the mechanisms behind catalyst activity and stability, observing the catalyst in the electrolyte environment and under the applied potential is necessary. The most used electrochemical techniques in electrocatalysis research are cyclic voltammetry (CV), chronopotentiometry (CP), chronoamperometry (CA), and electrochemical impedance spectroscopy (EIS); all offer information on catalyst activity and changes in activity during the lifetime as well as some information about phase transitions that are induced by oxidation/reduction processes [1–3]. In situ catalyst characterization is described as the application of spectroscopy techniques that are applied coupled to the electrochemical experiments. In this way, electrochemical and spectroscopic signals are obtained simultaneously. This gives spectroscopic data for a given electrocatalyst under reaction conditions relevant to catalytic operations. In situ characterization offers us a wider understanding of oxidation/reduction processes, phase transitions, and activity trends induced by electrical potential. Additional information about the correlation between structural details and catalytic activity and selectivity can be obtained by operando catalyst characterization. This combines the use of in situ spectroscopic measurements for the investigated catalysts with true operational catalytic conditions [4].

The structure of electrocatalysts based on layered double hydroxide (LDH) is closely related to the brucite structure—$Mg(OH)_2$. The representative electrochemically active LDH is $Ni(OH)_2$. It has a layered structure where layers are formed from $Ni(OH)_6$ octahedra, containing Ni^{2+} in its center, which is coordinated by six hydroxide anions (Figure 1a). Functional LDHs are commonly composed of different metal cations of different valences. By cationic substitution of the divalent metal ion with the trivalent ion or ion of higher oxidation state, the layers become positively charged. The general formula of the LDH

structure is presented as $(M^{2+}{}_{1-x}M^{3+}{}_{x}(OH)_2)(A^{z-}{}_{x/z} \times mH_2O)$, where M^{2+} and M^{3+} are divalent and trivalent metal ions, respectively, and A^{z-} is an anion. The trivalent metal ions are also placed in the center of the octahedra, which is coordinated by six OH^- groups. This results in sheets that are positively charged. Consequently, the interlayer space is filled with anions to compensate for the positive charge (Figure 1b).

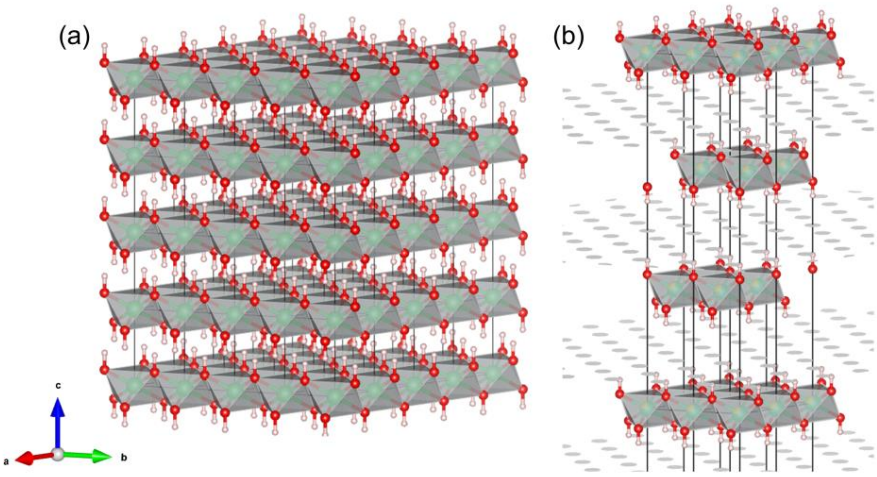

Figure 1. Presentation of layered LDH crystal structure. (**a**) Beta-nickel hydroxide visualized from PDF4+ #00-014-0117. (**b**) Iron nickel hydroxide with intercalated carbonate visualized from PDF4+ #01-082-8040. Ni^{2+}—green, Fe^{3+}—yellow, O^{2-}—red, H—white, intercalated carbonate layer—gray.

In electrochemical systems, the change in the valence of the metal ion is induced with electrochemical potential, and electrocatalytic reactions commonly proceed by electron transfer between the metal center and reactant. This induces structural changes in the LDH-based electrocatalysts (Figure 2), which are commonly associated with catalyst activity and stability [5,6]. A representative example is $Ni(OH)_2$, which consists of a mixture of nickel hydroxide sheets stacked into β-phase and anion-intercalated α-phase [7]. Oxidation of the Ni^{2+} to Ni^{3+} causes the β-$Ni(OH)_2$ to β-NiOOH [8]. At higher potentials, α-$Ni(OH)_2$ is oxidized to the γ-NiOOH phase, and β-NiOOH is further oxidized to γ-NiOOH with a maximum Ni average oxidation state +3.66 (Ni^{3+} is partially oxidized to Ni^{4+}) [9,10]. Such full oxidation is a predisposition for OER to take place [11–15]. The transformations between four phases are described by the Bode diagram (Figure 2) with α-$Ni(OH)_2$ and β-$Ni(OH)_2$ in the reduced state and β-NiOOH and γ-NiOOH in the oxidized state [16,17].

The $Ni(OH)_2$ oxidation/reduction sequence is of high importance as the phase transitions of other redox-active LDH materials are in general resembling $Ni(OH)_2$. Furthermore, the OER catalysts based on transition metals, metal oxides with perovskite and spinel structure, metal-chalcogenides (metal compounds with group 15 element), -pnictides (metal compounds with group 16 element), -carbides (metal compounds with carbon), and metal–organic frameworks commonly serve as precursors to metal (oxy)hydroxide [18–20]. The structure of α-, β-, γ-cobalt hydroxide is isostructural with α-, β-, γ-nickel hydroxide phases, respectively [21–23]. These parent structures are to some extent, with a reduced crystallinity and changed cell parameters, retained for the functional LDH materials that usually contain cationic substitution [24]. The substitutions can be intentional or originate from reagent impurities [12]. For example, the Co^{2+} substitution in β-$Ni(OH)_2$ causes the basal spacing to increase with increasing Co^{2+} content [25]. The substitution with ions in the trivalent state causes the need to compensate for the charge. If the β-structure is retained, charge compensation goes over proton removal and causes stacking faults [26]. In most cases, the charge is compensated by anion incorporation, and mixed metal LDH resembles the turbostratic α-$Ni(OH)_2$ structure, with defects in the stacking of hydroxide layers [17,27–31]. However, higher concentrations of M^{3+} ions can cause structure amorphization and even phase separation [32,33]. A similar oxidation cycle, with potential induced phase transitions, is also characteristic of $Co(OH)_2$, before the onset of the OER [34].

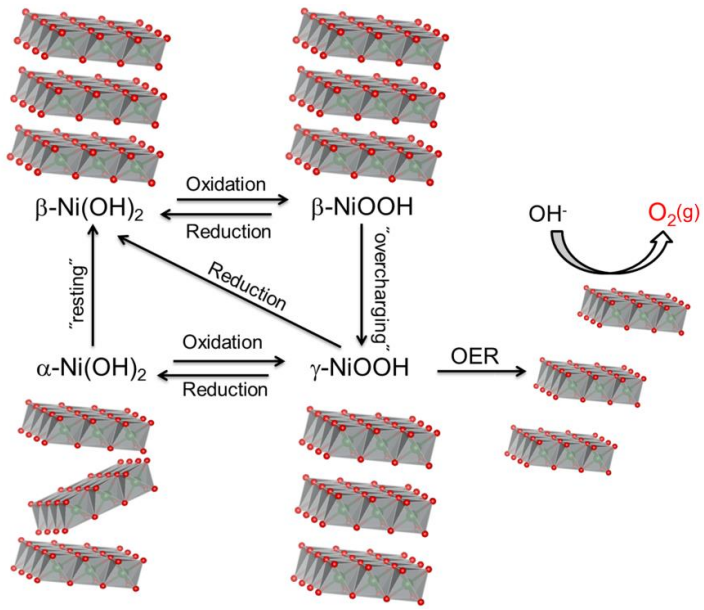

Figure 2. Illustration of Bode diagram. The phase transition routes as a function of the oxidation/reduction cycle. Adapted with permission from [5]. Copyright 2020 American Chemical Society.

The following sections will discuss the identification of phase transitions and reaction intermediates in LDH-based electrocatalysts for oxygen evolution reaction (OER). The application of in situ electrochemistry requires some adaptions of the experimental setup to allow light penetration (Figure 3). The cells can be designed with a working electrode prepared for transmission or reflection mode, with a counter and reference electrode away from the beam path. The electrolyte layer is usually thin to minimize light absorption, and the working electrode area is minimized to avoid inhomogeneous electric field distribution [35].

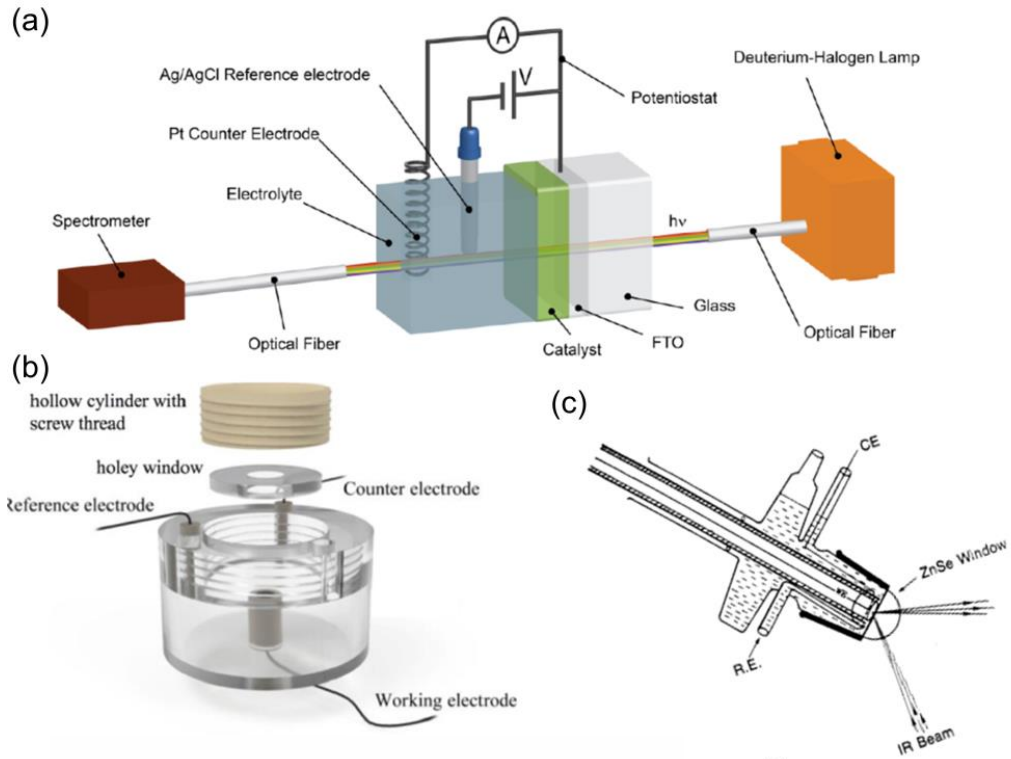

Figure 3. *Cont.*

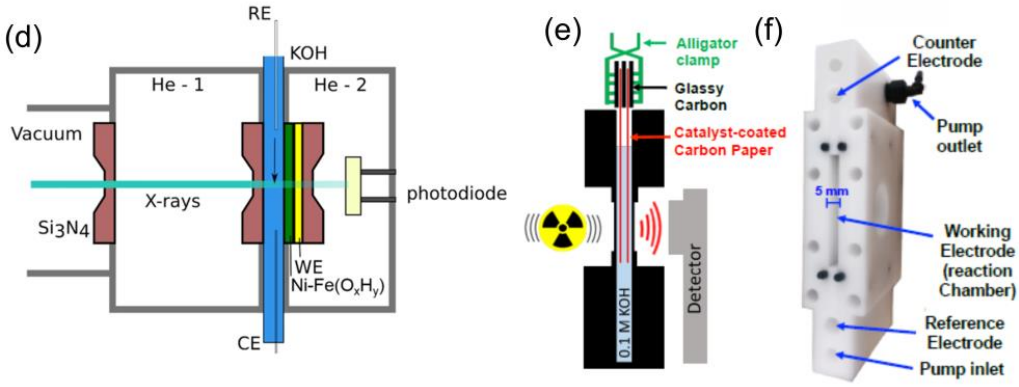

Figure 3. Schematic view of various electrochemical setups for the in situ measurements: (**a**) Cuvette for UV-Vis spectroscopy. Reprinted with permission from [36]. Copyright 2015 American Chemical Society. (**b**) Windowless cell for Raman spectroscopy. Reprinted from [37], Copyright 2020, with permission from Elsevier. (**c**) Cell for IR spectroscopy with ATR prism at the working electrode. Reprinted with permission from [38]. Copyright 1989 American Chemical Society. (**d**) Cell for X-ray Adsorption Spectroscopy (EXAFS and XANES) with Si_3N_4 windows placed in He gas to minimize X-ray adsorption. Reprinted from [39]. Copyright 2019, the authors. (**e**) Schematics of a cell for Mössbauer spectroscopy and (**f**) image of a cell for Mössbauer spectroscopy. Reprinted with permission from [40]. Copyright 2015 American Chemical Society.

2. In Situ UV-Vis

The change of the oxidation state or coordination environment in transition metal ions changes their electronic properties. The changes in the electronic structure can be followed by UV-Vis spectroscopy, which has been applied to Mn [41], Co [42], Fe [43] and most widely to study $Ni(OH)_2$, for which the difference in spectra for Ni^{2+} and Ni^{3+} is well resolved in different coordination environments (Table 1).

Ni^{2+} adsorbs UV light, and the α-$Ni(OH)_2$ has a peak at 305 nm, which shifts toward 290 nm during aging and the formation of β-$Ni(OH)_2$ [44]. The charging of Ni^{2+} to Ni^{3+}, accompanied by the phase transition, leads to the coloration of the electrode with a broad UV-vis absorption band centered at 450 nm [44,45]. This makes it widely applicable in electrochromic devices [46,47] and offers an opportunity to study $Ni^{2+/3+}$ redox behavior during electrochemical experiments. The broad peak in the visible region, corresponding to oxyhydroxide, can be resolved into three peaks. β-NiOOH adsorbs at 490–510 nm and 590–620 nm, whereas γ-NiOOH adsorbs at 430 nm [44,45]. Note that the average oxidation state in γ-NiOOH is 3.6 ± 0.1 due to the partial oxidation of Ni^{3+} to Ni^{4+} [45]. Further oxidation showed a red shift in adsorption toward 650 nm [48]. The reduction of Ni^{3+} (and Ni^{4+}) to Ni^{2+} causes a discoloration of the catalysts but is electrochemically quasi-reversible [5,44,45].

Table 1. Position of absorption peaks for Ni-(oxy)hydroxide species.

Ni Valence	Form	Wavelength (nm)	Reference
Ni^{2+}	Ni^{2+}(aq)	230–250	[49]
Ni^{2+}	α-$Ni(OH)_2$	305	[49]
Ni^{2+}	β-$Ni(OH)_2$	290	[49]
Ni^{3+}	β-NiOOH	490–510 and 590–620	[44,45]
$Ni^{3+/4+}$	γ-NiOOH	430	[44,45]
Ni^{4+}	β/γ-NiOOH	600–650	[48]

For the composite, bi-metallic hydroxides, where the second metal (e.g., Cd, Ce, Cr, Co, Cu, Fe, La, Pb, Mg, Mn, Ag, Y) cation is introduced into $Ni(OH)_2$, the absorption properties qualitatively resemble the behavior of Ni-hydroxide and -oxyhydroxide [50]. Fe^{3+} is frequently added to $Ni(OH)_2$ to increase its activity. While pure FeOOH during CV experiments does not show any adsorption changes in the range of visible light [51,52], the Ni oxidation/reduction behavior in NiFe-LDH materials can be studied uninterruptedly. Francàs et al. [43] used UV-vis to study Fe incorporation from FeOOH to sequentially deposited NiOOH. At first, Fe- and Ni-phase share only boundaries and are 'chemically pure'. Upon the oxidation of this mixture, the spectra resemble the FeOOH spectra (Figure 4a), indicating that Fe sites become charged and OER mainly takes place at Fe sites. This is in agreement with the higher activity of FeOOH compared to NiOOH [53]. Once NiFeOOH is formed by Fe intercalation, the UV-Vis spectrum upon oxidation resembles more the NiOOH spectra at lower Fe concentrations (<5%) and Fe spectra at higher Fe concentrations [43], whereas both Ni and Fe are oxidized at some middle Ni/Fe ratios. This is following the activity of different $Ni_{1-x}Fe_xOOH$ [12]. However, at higher potentials (1.5 V vs. RHE), an increase in adsorption at 430 nm has been observed for NiFeOOH films with a peak at 25% of Fe [54]. This increase was attributed to the oxidation of Ni^{2+} in di-μ-hydroxo Ni^{2+}-Fe^{3+}. A similar observation has been found by Goldsmith et al. [55] The adsorption becomes saturated before OER onset for pure $Ni(OH)_2$, while it continues to increase during the voltammetry sweep into the OER region for $Ni_{0.75}Fe_{0.25}O_xH_y$ (Figure 4b). This indicates that full oxidation of Ni is not necessary for the OER to proceed in NiFe-LDH catalysts. Görlin et al. [51] showed even more delayed adsorption, in the case of the $Ni_{0.45}Fe_{0.55}O_xH_y$ catalyst (note the higher Fe content), the coloration of the film only starts at OER onset. This is in agreement with CVs, where $Ni^{2+/3+}$ oxidation peaks cannot be resolved from the OER current [56]. Loos et al. [52] demonstrated the anodic shift of the $Ni^{2+/3+}$ oxidation peak and shift of light adsorption to the OER region for a series of $Ni_{1-n}Fe_nO_xH_y$ for $0 < n < 1$ (Figure 4c).

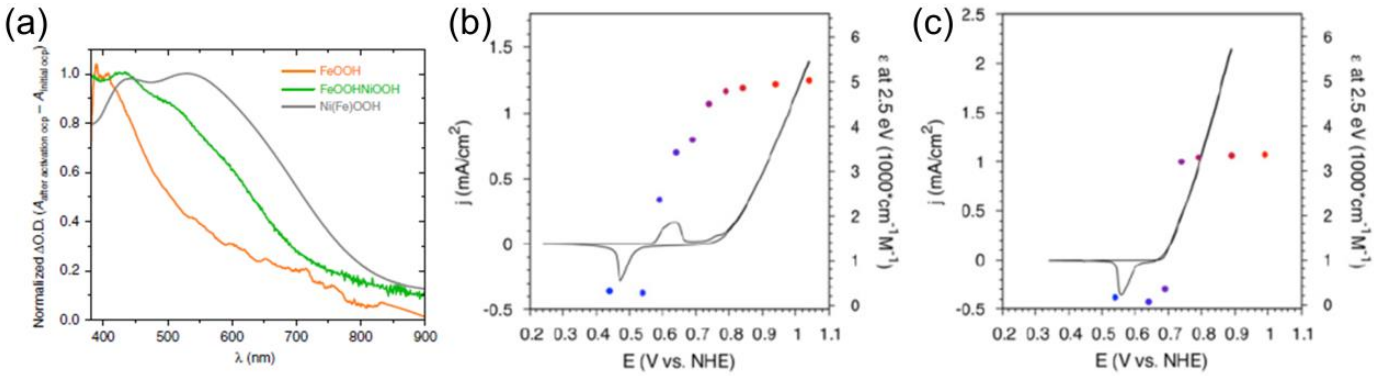

Figure 4. (**a**) Normalized adsorption spectra of FeOOH (orange), NiFeOOH (green), and NiOOH (gray) were obtained from the difference between the spectra at OCP before and after activation in the OER region. Reprinted from [43]. Copyright 2019 the authors. The CV (full lines) and potential-dependent extinction coefficient (dots) at 2.5 eV (496 nm) for (**b**) pure Ni-LDH and (**c**) $Ni_{0.75}Fe_{0.25}$-LDH. Reprinted with permission from [51]. Copyright 2017 American Chemical Society.

In situ UV-vis spectroscopy was used to follow the reversibility of Ni redox sites during the catalyst's lifetime for operation at high current density [5]. The adsorption during oxidation followed the position of the $Ni^{2+/3+}$ oxidation peak (Figure 5—green) and during the catalyst lifetime shifts to positive potential together with the oxidation peak. The discoloration of the catalyst started at the $Ni^{3+/2+}$ reduction peak onset and is completed at the peak offset for the as-prepared catalyst. During the catalyst lifetime, the position of the reduction peak offset did not change, but the adsorption decreases widened to the cathodic direction. When the catalyst was in a postmortem state, a voltage of 0.1 V vs. RHE needed to be applied to completely reduce the Ni^{3+} (Figure 5—red);

this indicates the high irreversibility of the $Ni^{2+/3+}$ redox couple as a result of structural changes induced by operation at high current density. The absorption of visible light is useful for resolving $Ni^{2+/3+}$ redox behavior. However, the light absorption properties of Ni-based-LDH catalysts need to be carefully considered when using those materials for photoelectrochemical devices, where high light adsorption of the catalyst layer might dramatically decrease the semiconductor performance.

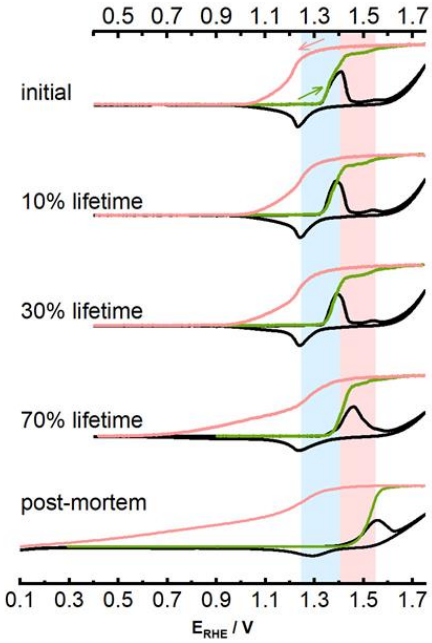

Figure 5. In situ UV−vis absorbance at 500 nm is associated with the forward (green) and backward (pink) scans at different lifetimes. Reprinted with permission from [5]. Copyright 2020 American Chemical Society.

In another application, UV-Vis absorption on a thin layer of the electrolyte has been applied to study the degradation rate of Ni-LDH in pure and Fe^{3+} spiked KOH. Monitoring the light adsorption at 230 nm (adsorption wavelength for Ni^{2+} ions), Wu et al. [49] showed that the catalyst does not dissolve at open circuit potential. At the OER potential, the catalyst in the absence of Fe^{3+} degrades faster. The higher stability of the Fe-containing catalyst is presumably due to the suppressed β-NiOOH to γ-NiOOH transition.

3. In Situ Raman Spectroscopy

Surface-enhanced Raman spectroscopy (SERS) makes it possible to obtain Raman spectra of oxides and hydroxides in electrolyte solutions with an acceptable signal/noise ratio. To enhance the Raman signal, plasmonic metal nanoparticles need to be applied as a substrate for the catalyst film. Gold particles with a diameter of around 100 nm give high enhancement factors [57] and form a relatively inert substrate from an electrochemistry perspective. However, the gold undergoes oxidation during electrochemical experiments that result in the potential dependent vibrational bands [58,59]. No features are recorded in Raman spectra, while gold is completely reduced. Increasing the potential to the 'capacitance' region results in a band for Au-OH at around 400–430 cm^{-1} that vanishes at the Au oxidation onset, where a band corresponding to Au-OH vibrations in the gold oxide at approximately 540 cm^{-1} appears. Note that the exact position depends on the electrolyte composition and pH. The O-H vibrations are present in the region 3000–3500 cm^{-1} but do not show potential dependence [58]. Upon reduction, gold-associated peaks vanish but need to be considered during SERS experiments on the Au substrate. This is of extreme importance for catalysts consisting of a few monolayers, where mixed oxides (e.g., NiAu oxide) can be formed [59].

Dried powder of bulk α-$Ni(OH)_2$ shows a main band at 465 cm^{-1} and weak features around 351, 376, 528, and 3585 cm^{-1}, and β-$Ni(OH)_2$ exhibits bands at 341 and 449 cm^{-1}, with weaker features at 376 and 516 cm^{-1} and a very strong band at 3580 cm^{-1} [9,60]. However, in water media, those features are absent or poorly resolved due to the low Raman scattering cross-section for these species [59–61]. A strong doublet in the region of Ni-OH vibrations is obtained upon the oxidation of hydroxide to oxyhydroxide with bands at ~480 and ~560 cm^{-1} (Figure 6a) [56,59–63]. Yeo et al. [59] studied the transformation of both phases, β-$Ni(OH)_2$/β-NiOOH and α-$Ni(OH)_2$/γ-NiOOH. For α/γ transition above 1.4 V vs. RHE, peaks appear at ~479 and ~558 cm^{-1} corresponding to γ-NiOOH. By increasing the potential, the peak ratio stays constant. For β/β transition, broad peaks at 475–477 cm^{-1} and ~556 cm^{-1} for β-NiOOH are observed at 1.4 V vs. RHE. These bands subsequently shift to 486 and 561 cm^{-1} as the potential is raised to 1.65 V vs. RHE, and the intensity of the peak at 560 cm^{-1} increases relative to 485 cm^{-1}. This indicates some sort of structural reordering within β-NiOOH but without the γ-NiOOH formation [59]. While β-NiOOH and γ-NiOOH bands are at approximately the same positions, in β-NiOOH, the ratio of 475/555 cm^{-1} is lower than in the case of γ-NiOOH [59,60]. From an experimental point of view, note that the stronger Raman resonance enhancement of a γ-NiOOH doublet is obtained under laser excitation of 633 nm (compared to 488 or 514 nm laser of equivalent laser power) [64], which is following γ-NiOOH adsorption of visible light (Figure 4a).

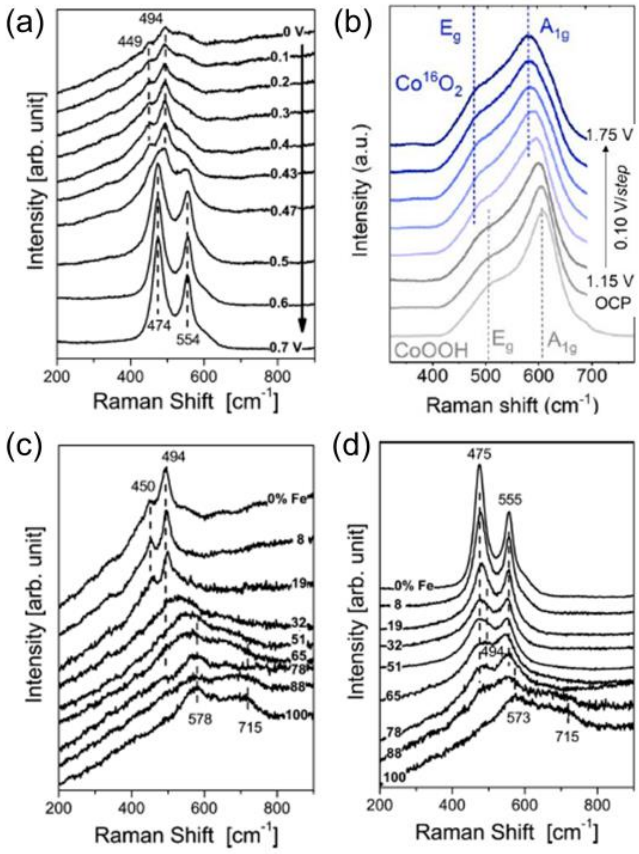

Figure 6. (**a**) In situ Raman spectra collected in the region of Ni-O vibrations. Ni films deposited on roughened Au substrate as a function of potential vs. Hg/HgO (1 M KOH) in 0.1 M KOH. Reprinted with permission from [56]. Copyright 2013 American Chemical Society. (**b**) In situ Raman spectra of CoOOH at increasing applied potential from OCP to 1.75 V (0.1 V per step) in 0.1 M Fe-free KOH. Reprinted with permission from [65]. Copyright 2020 American Chemical Society. (**c**,**d**) In situ Raman spectra collected for NiFe catalysts, as a function of composition, in 0.1 M KOH at a potential of (**c**) 0.2 V and (**d**) 0.6 V vs. Hg/HgO (1 M KOH) in 0.1 M KOH. Reprinted with permission from [56]. Copyright 2013 American Chemical Society.

Similarly to NiOOH, CoOOH also exhibits potential-dependent Raman vibrations [65,66]. The thin film of cobalt oxide at OCP with Co^{3+} shows a wide band centered at 608 cm^{-1} and a wider one at 508 cm^{-1}. The sharpness of the bands depends on the crystallinity of CoOOH films with sharper peaks present for more crystalline films [67]. After oxidation to Co^{4+}, those peaks are red-shifted and stabilized at 581 and 474 cm^{-1}, respectively (Figure 6b) [65].

A Raman signal is also obtained for a variety of FeOOH phases [68]. Under electrochemical conditions, a band at ~570 cm^{-1} is observed, and additional bands in the range 650–720 cm^{-1} may appear due to different iron oxides [56]. The band at ~570 cm^{-1} associated with the α-FeOOH does not show significant potential dependence as known for NiOOH. Nevertheless, the addition of Fe to NiOOH influences the Raman spectra. NiFe-LDH with different Ni/Fe ratios was studied by Louie and Bell [56]. At the onset of the OER (Figure 6c,d), the films with low Fe content (<20%) exhibit the sharp bands of $Ni(OH)_2$ (450 and 494 cm^{-1}) with a shoulder at ~530 cm^{-1}. At higher Fe contents, the sharp band disappears, while the broad band of $Ni(OH)_2$ (∼530 cm^{-1}) remains for intermediate Ni/Fe compositions and gradually shifts to ∼560 cm^{-1}. The disappearance of the sharp $Ni(OH)_2$ bands suggests that the NiFe-LDH structure is disordered. At higher Fe content, bands from the Fe phase are also visible (578 and 650–720 cm^{-1}), indicating a phase separation. At the onset of OER potential (Figure 6d), the doublet characteristic for NiOOH (at 475 and 555 cm^{-1}) is visible for films with as much as 90% Fe and is slightly red-shifted. However, the 555/475 peak ratio increases in intensity with Fe incorporation, which is correlated to an increased structural disorder of NiOOH. A higher 555/475 ratio indicates a higher structural disorder [13,56,69,70]. At Fe contents of 90% or higher, features associated with Fe phases at 573 and 650–720 cm^{-1} are observed. A similar doublet behavior was observed by Klaus et al. [13] during Fe incorporation by aging in unpurified (Fe-containing) KOH. Lee et al. [71] reported NiOOH characteristic doublet upon the oxidation of NiCo-LDH with 25% of Co. Bo et al. [72] studied ternary NiFeCr and CoFeCr oxyhydroxides. For NiFeCrOOH, it was shown that Cr addition promotes the formation of NiOOH doublet at a lower potential, which results in a lower overpotential for OER. The 555/475 peak ratio is increased for NiFeCrOOH compared to NiFeOOH, indicating that β-NiOOH is predominantly formed in the presence of Cr^{3+} [72]. Promotion of the formation of a NiOOH doublet was also observed for Ta-doped NiO [73]. Raman spectroscopy is also useful to monitor anion incorporation (e.g., nitrate [14,74], carbonate [75], borate [35]) or water [61].

The O-H stretching region of $Ni(OH)_2$ could be of interest as it allows differentiation between different phases [74]. However, in the presence of alkaline electrolytes and strong hydrogen bonding, it is distracted by electrolyte adsorption, which results in a broad feature between 3300 and 3600 cm^{-1} [9,60,74,76]. For an example of dry $Ni(OH)_2$ films, α-$Ni(OH)_2$ shows broad bands at 3659 and 3665 cm^{-1} with a shoulder at 3650 cm^{-1} [74]. In contrast, more crystalline β-$Ni(OH)_2$ exhibits sharp peaks at 3520, 3581, 3601, 3629, 3636, 3640, and 3652 cm^{-1} [74]. In wet films, the characteristic peak for α-$Ni(OH)_2$ is wide and located at ~3660 cm^{-1}, while for β-$Ni(OH)_2$, a sharp peak is present at ~3580 cm^{-1} [56,74]. Incorporating Fe into β-$Ni(OH)_2$ causes the disappearance of the sharp O-H vibration, indicating a change in the structure [13,56].

Another spectral region of interest not directly related to the LDH structure is the region between 900 and 1200 cm^{-1}, which is assigned to 'active oxygen' (Figure 7) [35,36,62,65,70,71]. 'Active oxygen' was first described as O^0 [61] and later assigned to superoxide species ($M\text{-}OO^-$) [62,65]. Broad multiple peaks in this region appear at the potential that is slightly higher for NiOOH formation [61,62]. The bands are present in strong alkaline electrolytes; their intensity increases with higher pH (an increase from pH 11 to 14) [35,62]. The presence of active oxygen was also found for NiFeOOH [35,70,71], NiCoOOH [71], and CoOOH [65]. Dissolved O_2 that is present at the OER potential was reported to give a weak signal at about 1550 cm^{-1} [73].

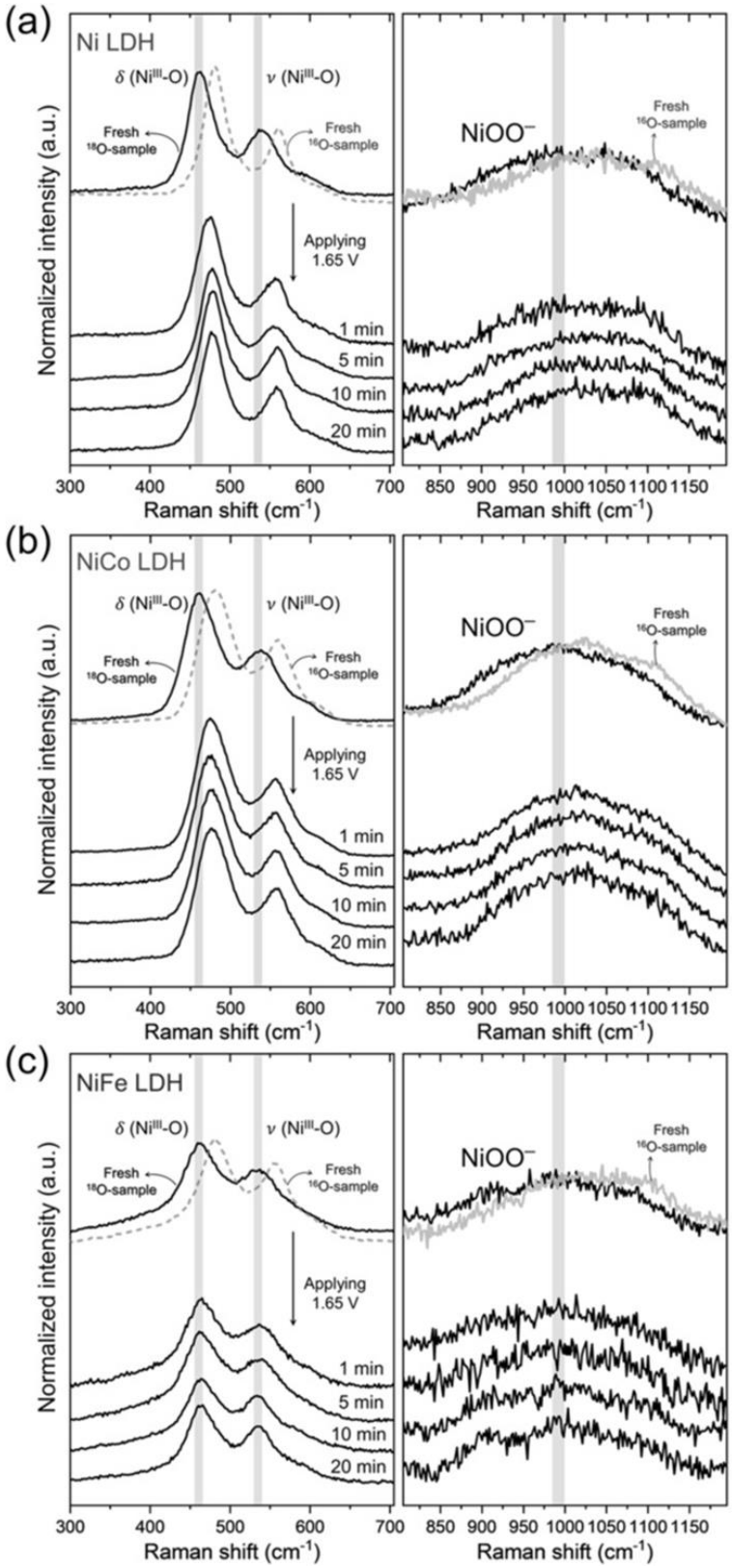

Figure 7. Isotope exchange experiments. In situ Raman spectra of ^{18}O labeled (**a**) Ni-LDH, (**b**) NiCo-LDH, and (**c**) NiFe-LDH measured at 1.65 V in 0.1 M KOH in $H_2{}^{16}O$. The Raman spectra were obtained in the regions of the Ni-O vibrations and the region of 'active oxygen' (right column). Reprinted from [71]. Copyright 2019 the authors.

The position of Raman bands depends on the energy of the bond, which can be slightly tuned using different isotopes. This keeps the chemical properties of the material the same but allows the tracking of 'isotope-labeled' species. For the isotope labeling of M-O bonds, ^{18}O (0.2% natural abundance) is used. Two approaches are found in the literature. The first approach is to operate metal hydroxide in $H_2{}^{18}O$ to follow the formation of active oxygen on the surface of metal oxide [62,65]. In this way, the superoxide (M-OO^-) nature of active oxygen was confirmed, during OER, ^{18}O is actively introduced from the electrolyte to the lattice of MOOH [65]. Another approach is to synthesize metal hydroxide and then run OER in $K^{18}OH$ prepared in $H_2{}^{18}O$ to force ^{18}O labeling [70,71]. The introduction of ^{18}O causes a Ni-O doublet of NiOOH to red-shift for approximately 50 cm^{-1}. Running OER on labeled catalyst materials shifts those peaks back to the original value for unlabeled hydroxides in the case of Ni-LDH and NiCo-LDH (25% Co), while there is no charge for NiFe-LDH (25% Fe) and NiCoFe-LDH (20% Co, 5% Fe) [71]. This indicates that lattice oxygen is involved in OER for Ni-LDH and Co-LDH, while in the presence of Fe, active sites for OER are Fe-related. The Fe concentration naturally plays a crucial role. At lower concentrations (i.e., 2.3%), the shift to original, unlabeled positions is somehow retarded, while at Fe > 4.6%, there is no shift to the original position [70]. Similar results were found for the region of active oxygen. While the red-shift after the isotope labeling of $NiOO^-$ is observed, in the case of Fe addition, ^{18}O is not exchanged, showing that $NiOO^-$ is not included in the OER process in the presence of Fe (Figure 7c) [70,71]. Note that these experiments were conducted under a low current regime (<10 mA cm^{-2}), and the possible involvement of lattice oxygen at a higher current density cannot be ruled out.

4. In Situ Infrared Spectroscopy

Infrared (IR) light can be absorbed by stretching or banding bonds, where a bond has a change in dipole moment. This makes IR spectroscopy complementary to Raman spectroscopy to obtain full vibrational information about the material. However, in situ IR spectroscopy for electrochemical systems is affected by the strong adsorption of water that interferes with the measurement of target vibrations. Nevertheless, the surface of the electrode can be measured with a thin film of electrolyte, or the catalyst thin films can be measured from the back in an attenuated total reflection Fourier transform-IR setup (ATR-FTIR), where light adsorption in the electrolyte is avoided (Figure 3c). Angle-resolved IR spectra can be used for the depth profiling of such thin films, allowing observations of bulk structure and structure at the electrode/electrolyte interface [37]. For $Ni(OH)_2$, O-H vibrations are present between 3650 and 3750 cm^{-1}, while in NiOOH, the energy of the O-H bond is lower between 3200 and 3400 cm^{-1}, and weak Ni-O vibrational starches are present between 400 and 525 cm^{-1} for both states [44,77]. Some distinction between β- and α-$Ni(OH)_2$ can be observed from IR spectra [37]. In the O-H stretch region, a sharp peak is observed for the β-phase (~3650 cm^{-1}), while a wide band is observed for the α-phase, corresponding to hydrogen-bonded water. A wide band for hydrogen-bonded water is also obtained for γ-NiOOH. In the Ni-O stretch, the infrared bands around 680 cm^{-1} are assigned to the α-phase, and bands around 513 and 457 cm^{-1} are assigned to the β-phase. In the oxidized state, both γ- and β-NiOOH show a band at 580 cm^{-1} with an additional peak at 4380 cm^{-1} for β-NiOOH [37].

Time-resolved infrared spectroscopy might be a useful tool for the characterization of surface intermediates during the catalytic reaction. Metal-oxyl, -oxo, -hydroxy, and -superoxide intermediates have been identified during photocatalytic reactions on the surface of different metal oxides [78]. The application of this technique in electrocatalysis might exploit the sequential molecular transformations on the surface from adsorbed water molecules to the release of O_2, with resolution down to 10 ns [78].

5. In Situ X-ray Absorption Spectroscopy

X-ray absorption spectroscopy (XAS) allows element-specific observations of the metal oxidation state and the distribution of neighboring atoms. Careful modifications of measurement cells (see for example Figure 3d) need to consider minimizing X-ray adsorption to allow observing the catalysts in situ and operando mode. XAS is extremely useful to investigate any phase changes occurring at higher potentials where redox processes are overlapping and are hard to resolve by electrochemical techniques. Changes in the oxidation and metal–oxygen bond distance are observed while the potential increases and cycles back (Figure 8a). In situ X-ray Absorption Near Edge Fine Structure (XANES) spectra as a function of the applied potential show that the K-edge shift for octahedral nickel ions can be connected with the change in the oxidation state. It increases linearly at 1.55 eV per oxidation state [79,80], and the pre-edge changes at 0.6 eV per oxidation state [79]. Consequently, the oxidation state can be obtained for specific $Ni_{1-x}Fe_x$-LDH composition (Figure 8b) [54]. Depending on the deposition method, prepared films can be purely Ni^{2+} [81] or partially oxidized to Ni^{3+} [54]. Applying oxidative potential induces Ni^{2+} oxidation. At the OER, pure Ni-LDH becomes oxidized to a mixture of Ni^{3+} and Ni^{4+} in γ-NiOOH, and no further phase transition is observed up to ~1.7 V vs. RHE [15]. The addition of Fe^{3+} to form NiFe-LDH impacts the redox behavior of the $Ni(OH)_2$ matrix. It shifts $Ni^{2+/3+}$ oxidation to higher potential and at the same time reduces the potential for OER, causing the overlap of those two redox processes. Incorporated Fe is present as Fe^{3+}, independent of the amount of Fe added and applied potential (Figure 8c) [50,54,80,81]. Fe^{3+} plays a role in stabilizing Ni^{2+} and inhibiting oxidation, with a large amount of Ni^{2+} at the potential of OER (Figure 8d) [35,80–83]. The presence of a mixture of $Ni^{2+/3+/4+}$ was also shown with soft X-ray adsorption at Ni L_3-edge [84]. This indicates the presence of electrochemically active and bulk Ni sites. One needs to note that XAS is not a surface-sensitive technique, and obtained data come from the surface that is actively involved for OER and from the bulk of the electrodes.

To avoid the effect of the bulk electrode material, Kuai et al. [85] analyzed ultrathin NiFe-LDH with metal ions fully exposed to the electrolyte. For low OER overpotentials, they show that both Ni and Fe in ultrathin LDH can be fully oxidized into a tetravalency state, which facilitates the lattice-oxygen-involved OER. This finding indicates that the complete oxidization of metal ions is a prerequisite for highly active LDH-based OER catalysts, and lower-valence metal ions are in the bulk of electrode material. The oxidation state of Ni decreases with increasing Fe^{3+} content [54]. For Fe levels below ~25%, the oxidized catalyst can be described as γ-$Ni_{1-x}Fe_xOOH$, reflecting the substitution of Ni by Fe cations. In this form, the Ni-O and Fe-O bond distances analyzed by Extended X-ray Absorption Fine Structure (EXAFS) are very similar, and both are comparable to the Ni-O bond distance in γ-NiOOH [81,82]. The fitting of EXAFS was able to demonstrate the difference in coordination number and disorder for 2D and bulk catalysts, indicating the vacancies in delaminated 2D catalysts [86].

The intercalation of Na^+ in the NaOH electrolyte was confirmed in γ-NiFeOOH recording Na K-edge spectrum, indicating the disordered structure [84]. The Na^+ concentration increases as the Ni and Fe valence states increase. A comparison of the EXAFS spectra collected at pre-OER potential and OER potential for Ni and Fe shows similar modifications of the first coordination sphere, i.e., shorter M-O distances in the oxidized state, and the second coordination sphere, i.e., shorter M-M distances in the oxidized state (Figure 8e) [81,82,87]. As the Fe level rises above 25%, the XAS data suggest that a γ-FeOOH phase nucleates, containing no or <3% Ni [81]. The nucleation of a separated FeOOH phase has also been observed under operational conditions at high current density [87], which is presumably to relieve the lattice distortion.

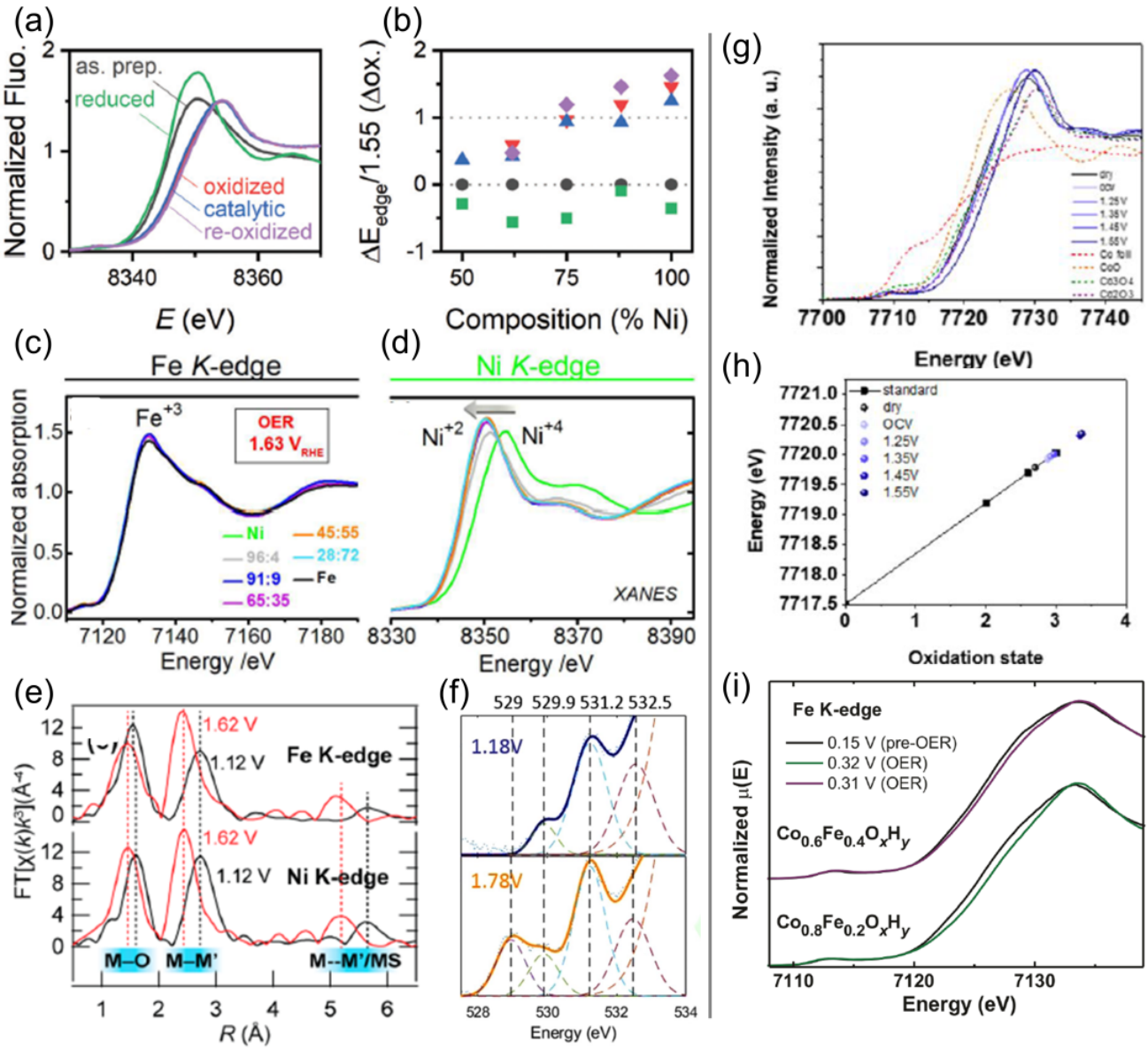

Figure 8. (**a**) Voltage-dependent XANES for the Ni K-edge of pure NiO_x and (**b**) normalized relative shifts in the Ni K-edge for the composition series giving the oxidation state change relative to the as-prepared sample for each composition. Data for as-prepared (black), oxidized (red), catalytic (blue), reduced (green) and re-oxidized (purple) films. Used with permission of Royal Society of Chemistry, from [54]; permission conveyed through Copyright Clearance Center, Inc. XAS spectra of the NiFe catalysts with varying catalyst composition ($Ni_{1-x}Fe_x$) freeze-quenched under application of catalytic potential after conditioning at 1.63 V for 30 min in 0.1 M KOH: (**c**) Fe K-edges and (**d**) Ni K-edges. Reprinted with permission from [80]. Copyright 2016 American Chemical Society. (**e**) Fourier transform EXAFS measurement on Fe and Ni K-edge confirming the potential-induced bond contraction at both Fe and Ni sites. Reprinted with permission from [81]. Copyright 2015 American Chemical Society. (**f**) O K-edge pre-edge region spectra of electrodeposited Ni-Fe catalyst measured at 1.18 V and 1.78 V vs. RHE. Reprinted from [39]. Copyright 2019, the authors. (**g**) XANES spectra of CoOOH at various potentials, and reference samples Co foil (red), CoO (brown), Co_3O_4 (green), and Co_2O_3 (purple), and (**h**) corresponding linear relationship of the oxidation state. Reprinted with permission from [65]. Copyright 2020 American Chemical Society. (**i**) Operando Fe K-edge XANES data at different overpotentials. OER XAS data were collected at the potentials necessary to maintain 3–4 mA cm^{-2}. Reprinted with permission from [88]. Copyright 2018 Wiley-VCH Verlag GmbH & Co.

Drevon et al. [39] studied the voltage-dependent changes of the O K-edge to evaluate the state of oxygen during OER for an electrodeposited $Ni_{0.65}Fe_{0.35}O_xH_y$. A pre-peak appears on the O K-edge (Figure 8f) simultaneously with a process, corresponding to the formation of oxidized $Ni^{3+/4+}$, but before O-O bond formation and before the OER onset. The additional pre-peak is associated with the presence of oxidized Ni. It implies increased hybridization between O 2p and Ni 3d and induced charge transfer from O to Ni. This gives rise to an electron-deficient oxygen site, which is assigned to the pre-peak at 529 eV. It is hypothesized that these sites are likely to arise from under-coordinated O sites found at edge or defect sites of the oxyhydroxide layers; however, their role in the OER activity was not analyzed.

CoOOH shows an increase in the oxidation potential with the applied potential in a similar way as NiOOH. Initially, dry CoOOH mostly consists of Co^{3+} mixed with some Co^{2+} [65]. After immersing the CoOOH in the electrolyte, the average oxidation state of Co ions slightly increases. The average oxidation state of Co ions gradually increases with increasing applied potential, which is followed by a sharp increase at 1.45 V corresponding to the oxidation of a part of Co^{3+} to Co^{4+} (Figure 8g,h) [42,65]. Furthermore, EXAFS reveals that increasing the potential changes the coordination number of Co from about 5.5 to 6.0. This indicates that at the initial stage, the catalyst contains a mixture of 4- or 5-coordinated Co^{2+} and 6-coordinated Co^{3+}. After Co^{2+} becomes fully oxidized, the coordination number stays at 6.0 regardless of the potential increase. This is attributed to a similar structure between Co^{3+} and Co^{4+} oxyhydroxides, with no significant change in the coordination number as well as the interatomic distance [65]. Interestingly, the voltage dependence of the position of the absorption edge is found to differ for the experiments in D_2O and H_2O, where CoOOH samples conditioned in D_2O attain a lower average oxidation state at the same applied potential [89].

The introduction of iron to the CoOOH matrix structure causes a change in the Co^{2+}/Co^{3+} ratio. As the Fe content increases, the Co average oxidation state decreases while Fe is present as Fe^{3+} [42]. However, at the OER onset, Co is fully present in Co^{3+}, and further oxidation to Co^{4+} is largely suppressed [88]. In the OER region, Fe^{3+} is further oxidized (Figure 8i). It is suggested that Fe^{3+} oxidizes to Fe^{4+}, Fe^{5+}, or Fe^{6+} [88].

In addition to in situ measurements, XAS is of extreme importance when analyzing catalysts that are amorphous to XRD. The Ni-, Co- and Mn-oxyhydroxide thin films deposited from solution during OER are generally too irregular to be analyzed by XRD; however, XAS analysis allows us to understand its structure. The structure is familiar to the LDH structure. Although the metal oxides are amorphous, they consist of metal ions octahedrally coordinated to six oxygen atoms with neighboring cations bound through di-μ-oxido bridging to yield 2D sheets but no detectable mono-μ-oxido bridging between the redox-active metal ions. The catalyst layers contain water and anions [90,91]. The Ni oxide layer deposited during OER incorporates the most water and anions. It consists of NiOOH with a mixture of Ni^{3+} and Ni^{4+}, indicating that the structure of Ni oxide deposited at OER conditions strongly relates to γ-NiOOH [90].

6. In Situ Mössbauer Spectroscopy

Mössbauer spectroscopy is based on the emission and absorption of γ-photons that have high penetrating power. This makes the technique highly suited for the characterization of catalysts under operating conditions as radiation can travel through the bulk catalyst (Figure 3e,f). The technique is based on the Mössbauer effect, indicating the resonant, recoil-free absorption of nuclear radiation. This means that the atoms in the source emitting the γ-rays must be of the same isotope as the atoms in the sample absorbing them. This limits the possibility of suitable source–analyte pairs. The most commonly studied isotope is ^{57}Fe with ^{57}Co radiation sources; the method yields information on oxidation states, magnetic properties, and lattice symmetry and has been widely applied for catalysis [92].

Although limited to a small number of elements, Mössbauer spectroscopy has been used for NiFe- and Fe-oxyhydroxides by enriching the material with a ^{57}Fe isotope [39]. The ^{57}Fe Mössbauer spectra were recorded at a different potential from the OCP to the OER region (Figure 9). An initial spectrum of the NiFe-oxyhydroxide catalyst at OCP conditions shows a doublet at positions characteristic of Fe^{3+} (Figure 9b). There is no change in the spectrum up to $Ni^{2+/3+}$ oxidation onset (Figure 9c). A change in the spectrum is found significantly in the OER region where a shoulder at the position of Fe^{4+} appears (Figure 9d), increasing the potential further to the OER region and resulting in a growth of the Fe^{4+} peak, accounting for approximately 21% of the total Fe (Figure 9e). When the potential is reversed, the Fe^{4+} peak is still evident (Figure 9f) and is maintained for up to 48 h when the catalyst is kept at OCP (Figure 9g). However, for pure Fe-oxyhydroxide, no Fe^{4+} is detected during the OER potential (Figure 9h–j), indicating that the presence of Ni-ions stabilizes the Fe^{4+} state [40]. Based on the identification of Fe^{4+} in NiFe-LDH, Chen et al. [40] concluded that due to the higher population of electrons in d-orbitals of Ni^{3+} compared to Fe^{3+}, the oxidation to higher valent Fe^{4+} is favorable in the NiOOH lattice, as lone pairs of Ni^{3+} can stabilize the structure over bridging oxygen atoms. Complementary, the $Ni^{2+/3+}$ oxidation potential in NiFe-LDH is increased as Fe^{3+} ions in the second coordination sphere make bridging oxide and/or hydroxide ligands less electron-donating, thereby destabilizing Ni^{3+} species in the NiOOH lattice.

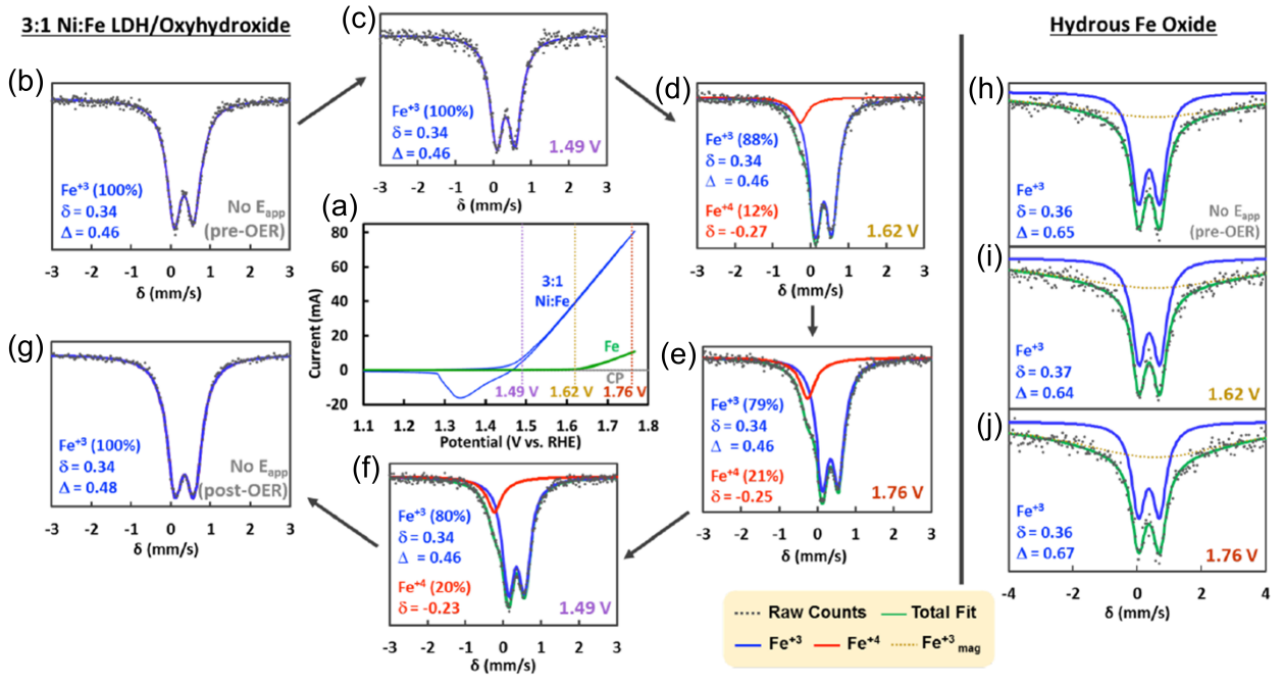

Figure 9. (**a**) CVs of NiFe and Fe-LDH. Mössbauer spectra were collected at the different potentials for (**b**–**g**) NiFe-LDH and (**h**–**j**) for Fe-LDH. Reprinted with permission from [40]. Copyright 2015 American Chemical Society.

7. Miscellaneous In Situ Techniques

7.1. Online Application of Mass Spectrometry

Electrocatalyst degradation during oxidation conditions due to dissolution is one of the main challenges in OER catalyst design. Online inductively coupled plasma mass spectrometry (ICP-MS) allows following the corrosion of metals from the catalyst with the lower detection limit for ICP-MS extending to parts per trillion (ppt). This gives an option of time- and potential-resolved monitoring of the rate of catalyst dissolution and identification of metals that are prone to dissolution. The method has been commonly applied for state-of-the-art RuO_2/IrO_2 OER catalyst systems to determine the effect of support, particle sizes, and crystallographic orientation on the potential dependent dissolution rate [93–95].

Mass spectrometry can be also applied to follow oxygen evolution using differential electrochemical mass spectrometry (DEMS). DEMS allows us to precisely follow the amount of released oxygen and to calculate potential-dependent faradaic efficiency during a cyclic voltammetry scan [96,97]. It was confirmed that NiFe- and CoFe-LDH catalysts are oxidized before OER takes place (Figure 10a), and the faradic efficiency for OER during the first cycle is always lower compared to later cycles [50,98]. Isotope labeling experiments can also distinguish the OER mechanism pathway. Roy et al. [99] discussed different procedures to perform ^{18}O labeled experiments. Firstly, NiFe-hydroxide is prepared by oxidation in 0.1 M $K^{16}OH$, and OER is run in 0.1 M $K^{18}OH$. Since ^{18}O purity in water is only 97%, the ratio between ^{16}O-^{18}O and ^{18}O-^{18}O oxygen needs to be followed to investigate the origin of ^{16}O. Alternatively, starting from NiFe metal nanoparticles, the labeled hydroxide can be made by the electrochemical oxidation of metal in 0.1 M $K^{18}OH$ or by thermal oxidation at 450 °C in the vacuum chamber in the presence of $^{18}O_2$ gas. The ^{18}O labeled hydroxides are more sensitive to determine lattice exchanged O, but the real isotopic composition of hydroxide is uncertain due to the presence of ^{16}O in the mixture with ^{18}O. For NiFe-hydroxide films, the association mechanism was confirmed as the predominant mechanism. The lattice oxygen is more involved for OER when using pure $Ni(OH)_2$, which is in line with in situ Raman results [99,100].

7.2. Scanning Electrochemical Microscopy

In Scanning Electrochemical Microscopy (SECM), an ultramicroelectrode tip (UME) immersed in a solution is moved above a substrate surface. The products that are electrogenerated at the substrate are detected at the tip. This allows the direct detection of the reaction intermediates in an electrolyte environment [101]. Depending on the tip size, the spatial resolution ranges from ~10 μm to nm-scale [102].

To quantify the number of surface-active sites accessible to water molecules, a modified method has been developed. In Surface Interrogation Scanning Electrochemical Microscopy (SI-SECM), an SECM tip is used to generate in situ a titrant from a reversible redox pair that reacts with the adsorbed species at the substrate [103–105]. Ahn and Bard [103] applied SI-SECM to investigate the kinetics of active sites in $Ni_{1-x}Fe_xOOH$. Two size-matched UME were placed at a distance of 2.0 μm; at this position, a tip-generated analyte is quantitatively detected at the substrate with the deposited catalyst film (Figure 10b). The redox mediator was a triethanolamine (TEA) complex of iron with $FeTEA^{-/2-}$ standard reduction potential at −1.05 V vs. Ag/AgCl in 2 M NaOH. At the beginning of the experiment, both electrodes (tip and substrate) are at OCP potential. The redox mediator is in its oxidized state ($Fe^{III}TEA^-$), and the nickel atoms in the catalyst film are in Ni^{2+} states. As the substrate electrode is pulsed to more positive potentials, the oxidation states of nickel reach 3+ or 4+ (Figure 10c). After a certain delay time, the redox mediator is reduced at the tip by the application of negative potential. This introduces the titrant ($Fe^{II}TEA^{2-}$) (Figure 10d). The titrant reduces Ni^{3+} and Ni^{4+} back to Ni^{2+}, which decreases the tip current for the reduction of $Fe^{III}TEA^-$ back to the background level at negative feedback upon the consumption of surface-active species. In this way, the number of surface-active species can be determined. The reaction rate constants of active sites can be determined by varying the time between active species production and the tip generation of the titrant. The titration current should decay as a function of delay time as water oxidation consumes the active sites in the absence of the titrant. They observed high densities of surface catalytic sites of $Ni(OH)_2$, FeOOH, and $Ni_{1-x}Fe_xOOH$ electrodes (~300 atoms nm^{-2}). The density of surface sites is for an order higher than in, for example, Co-oxyhydroxide [105]. This suggests that also atoms from the bulk might participate in the surface catalysis via fast hole conduction through the catalyst film in Ni-based LDH catalysts. Time-dependent titrations for the study of reaction kinetics show that NiOOH is a poor OER catalyst, and pure FeOOH also shows poor OER kinetics. In the $Ni_{1-x}Fe_xOOH$ electrode, fast and slow sites were observed. The fast-active sites belong to the dispersed iron atoms in a NiOOH matrix, and the reaction constant increases with iron content up to 25%, where phase segregation into NiOOH and FeOOH was observed and decreased the reaction rate more than five times, which indicates the importance of homogenous iron distribution.

Using a transparent substrate electrode, Steimecke et al. [69] coupled Raman spectroscopy with SECM, which provides spectroscopic and electrochemical information of the very same location of an electrode at the same time. This allowed decoupling of the OER onset potential by the detection of evolved O_2 on Pt UME from $Ni(OH)_2$ to NiOOH transition identified by spectroscopic data, which is overlapping in cyclic voltammograms for NiFe-LDH with higher Fe content. The lowest OER onset potential was found for the film containing 15%Fe in Ni/Fe. The potential-dependent formation of γ-NiOOH characterized by Raman spectroscopy shows that by increasing the Fe content, γ-NiOOH formation is shifted to higher potential; besides, a decrease of the 475/557 cm^{-1} peak ratio indicates that a certain amount of disorder introduced by Fe atoms is necessary to obtain high OER activity.

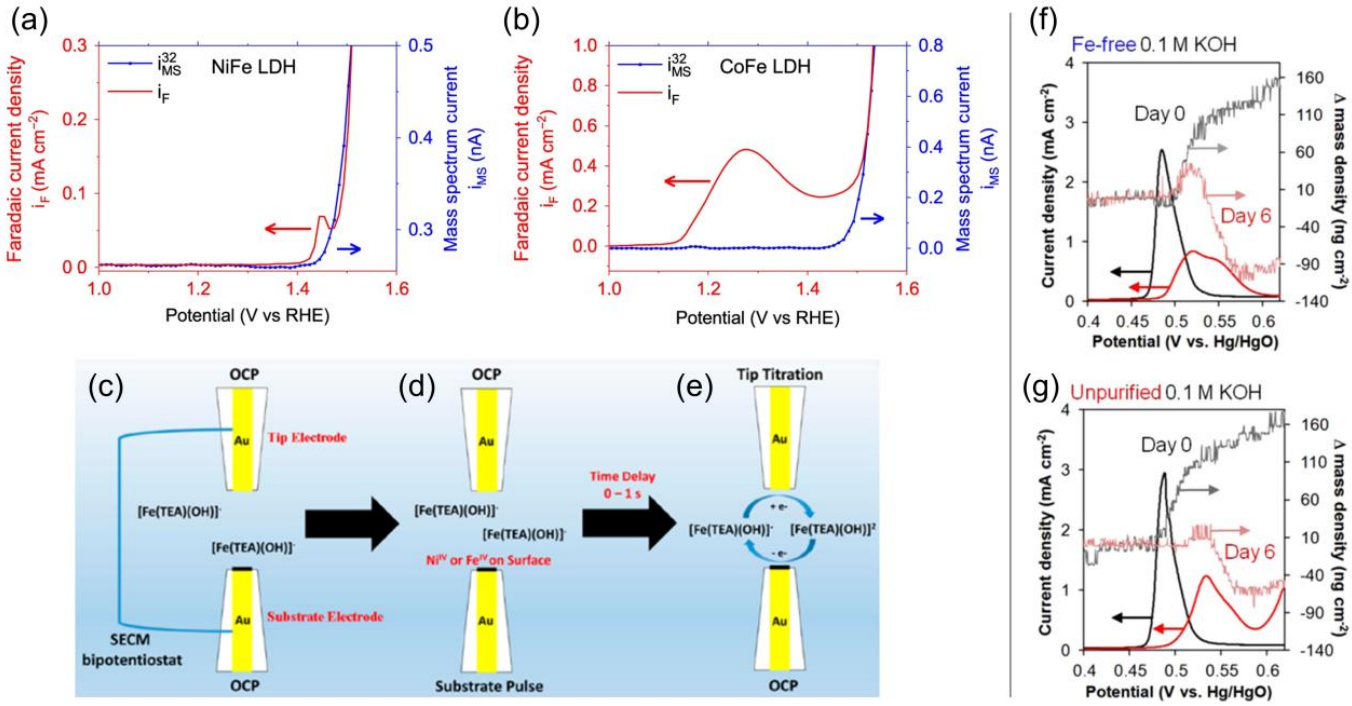

Figure 10. DEMS measurement (blue) of (**a**) NiFe-LDH and (**b**) CoFe-LDH during a linear sweep voltammetry (red) in 0.1 M KOH. The mass spectrum current related to m/z = 32 for O_2 detection reprinted from [98]. Copyright 2020, the authors. Titration scheme of SI-SECM: (**c**) Tip and substrate electrode at OCP potential. (**d**) Pulse on the substrate electrode to form active species. (**e**) After a fixed delay time, the pulse on the tip electrode forms a titrant. Reprinted with permission from [105]. Copyright 2016 American Chemical Society. EQCM mass density change as a function of applied potential (potential scans at 10 mV s^{-1}) for $Ni(OH)_2$ films deposited on Au/Ti quartz crystals in (**f**) Fe-free and (**g**) unpurified 0.1 M KOH before and after 6 days of aging. Reprinted (adapted) with permission from [13]. Copyright 2015 American Chemical Society.

7.3. Electrochemical Quartz Crystal Microbalance

Using Electrochemical Quartz Crystal Microbalance (EQCM), one can simultaneously obtain mass changes as a result of electrochemical processes. The method was extensively used with $Ni(OH)_2$ electrodes for batteries to investigate the effect of conditions for thin film deposition, the transfer of H^+ or OH^- during the redox process, and the incorporation of anions and other metal cations, and it has been thoroughly reviewed previously [106]. However, technical limitations such as the disturbance of mass measurement due to bubble evolution or oxidation of electrode and electrode contact in harsh electrolyte environments at high oxidative potentials limit its use in water oxidation electrocatalysis. EQCM is used to differentiate between the oxidation of a- to g-phase and b- to b-phase. An increase in film

mass occurs during the oxidation of α-$Ni(OH)_2$ to γ-NiOOH as a result of the intercalation of water and ions, while the oxidation of β-$Ni(OH)_2$ to β-NiOOH does not change the mass or results in mass loss.

Klaus et al. [13] used EQCM to track the conversion of α-$Ni(OH)_2$ to β-$Ni(OH)_2$ with aging in Fe-free and unpurified KOH. For $Ni(OH)_2$ films initially cycled in both Fe-free and unpurified 0.1 M KOH, the mass increases for ~160 ng cm^{-2} as a result of $Ni(OH)_2$ oxidation to NiOOH. Samples aged 6 days exhibit a decrease in mass uptake upon oxidation. Mass is increased for ~110 ng cm^{-2} and ~50 ng cm^{-2} for aging in purified and unpurified KOH, respectively (Figure 10f,g). This indicates that aging in unpurified electrolytes stabilizes the α-$Ni(OH)_2$. Although some amount of β-NiOOH is formed after aging in the unpurified electrolyte, it is significantly less than the amount formed in the Fe-free electrolyte.

8. Conclusions

The electrochemical processes occurring in transition metal-based LDH catalysts have been found to induce changes in their oxidation state and coordination environment. By combining spectroscopy techniques with electrochemical experiments, it becomes possible to track these changes in oxidation state and structure. UV-Vis spectroscopy has been extensively utilized to investigate the alterations in the electronic structure of metal ions, which directly correlates with changes in their oxidation number and coordination environment. Raman spectroscopy, in conjunction with electrochemical reactions, has provided valuable insights into the structural transformations and phase transitions of metal oxides and hydroxides. Vibrational spectroscopy, particularly with isotope exchange experiments, has shed light on the involvement of lattice oxygen in these processes. In situ X-ray absorption spectroscopy (XAS) has enabled the observation of metal oxidation states and the distribution of neighboring atoms during electrochemical reactions. XAS studies have unveiled changes in oxidation states and metal–oxygen bond distances as the potential increases, highlighting the influence of guest metal ion incorporation on the redox behavior of the host LDH structure. Moreover, XAS data have allowed for the differentiation between electrochemically active and inactive bulk metal sites. In situ Mössbauer spectroscopy has provided a means to characterize Fe-containing catalysts under operating conditions, offering insights into the oxidation states of Fe and the nature of active sites.

The combination of various spectroscopy techniques with electrochemical experiments has provided a deep understanding of the changes occurring in oxidation state and coordination environment within transition metal-based LDH catalysts. These insights are invaluable for the design and optimization of more efficient and durable catalyst materials for electrochemical water oxidation. However, when operating at high current densities, these methods face limitations that hinder their effectiveness. Electrochemical interference, such as the formation of gas bubbles and changes in local pH, can disrupt the catalyst's environment and interfere with spectroscopic measurements. Gas bubbles, for instance, can physically obstruct the light path in optical spectroscopy or impede the access of probe molecules in vibrational spectroscopy. High current densities also generate increased heat, causing local temperature gradients that impact temperature-sensitive techniques such as Raman and IR spectroscopy. Additionally, cell design plays a crucial role as it needs to establish an optical path for most spectroscopy methods. Consequently, the transport of reactants and products to and from the electrode surface becomes challenging at high current densities due to limited mass transport, resulting in concentration gradients. To address these challenges, cell designs should promote efficient mass transport, such as employing appropriate flow cells or microfluidic systems to ensure a well-mixed electrolyte environment.

Author Contributions: Conceptualization, A.M.; validation, A.M. and M.V.; writing—original draft preparation, A.M.; writing—review and editing, A.M. and M.V.; visualization, A.M.; funding acquisition, A.M. and M.V. All authors have read and agreed to the published version of the manuscript.

Funding: This research was funded by the Slovenian Research Agency, grant numbers P2-0412, and J2-2498.

Data Availability Statement: No new data were created or analyzed in this study. Data sharing does not apply to this article.

Conflicts of Interest: The authors declare no conflict of interest.

References

1. Stevens, M.B.; Enman, L.J.; Batchellor, A.S.; Cosby, M.R.; Vise, A.E.; Trang, C.D.M.; Boettcher, S.W. Measurement Techniques for the Study of Thin Film Heterogeneous Water Oxidation Electrocatalysts. *Chem. Mater.* **2017**, *29*, 120–140. [CrossRef]
2. Anantharaj, S.; Kundu, S. Do the Evaluation Parameters Reflect Intrinsic Activity of Electrocatalysts in Electrochemical Water Splitting? *ACS Energy Lett.* **2019**, *4*, 1260–1264. [CrossRef]
3. Anantharaj, S.; Noda, S. Appropriate Use of Electrochemical Impedance Spectroscopy in Water Splitting Electrocatalysis. *Chemelectrochem* **2020**, *7*, 2297–2308. [CrossRef]
4. Banares, M.A. Operando methodology: Combination of in situ spectroscopy and simultaneous activity measurements under catalytic reaction conditions. *Catal. Today* **2005**, *100*, 71–77. [CrossRef]
5. Mavrič, A.; Fanetti, M.; Lin, Y.; Valant, M.; Cui, C. Spectroelectrochemical Tracking of Nickel Hydroxide Reveals Its Irreversible Redox States upon Operation at High Current Density. *ACS Catal.* **2020**, *10*, 9451–9457. [CrossRef]
6. Mavric, A.; Cui, C. Advances and Challenges in Industrial-Scale Water Oxidation on Layered Double Hydroxides. *ACS Appl. Energy Mater.* **2021**, *4*, 12032–12055. [CrossRef]
7. Hall, D.S.; Lockwood, D.J.; Bock, C.; MacDougall, B.R. Nickel hydroxides and related materials: A review of their structures, synthesis and properties. *Proc. R. Soc. A* **2015**, *471*, 20140792. [CrossRef]
8. Oliva, P.; Leonardi, J.; Laurent, J.F.; Delmas, C.; Braconnier, J.J.; Figlarz, M.; Fievet, F.; Guibert, A.d. Review of the structure and the electrochemistry of nickel hydroxides and oxy-hydroxides. *J. Power Sources* **1982**, *8*, 229–255. [CrossRef]
9. Desilvestro, J.; Corrigan, D.A.; Weaver, M.J. Characterization of Redox States of Nickel Hydroxide Film Electrodes by In Situ Surface Raman Spectroscopy. *J. Electrochem. Soc.* **1988**, *135*, 885–892. [CrossRef]
10. Van der Ven, A.; Morgan, D.; Meng, Y.S.; Ceder, G. Phase Stability of Nickel Hydroxides and Oxyhydroxides. *J. Electrochem. Soc.* **2006**, *153*, A210–A215. [CrossRef]
11. Huang, J.; Li, Y.; Zhang, Y.; Rao, G.; Wu, C.; Hu, Y.; Wang, X.; Lu, R.; Li, Y.; Xiong, J. Identification of Key Reversible Intermediates in Self-Reconstructed Nickel-Based Hybrid Electrocatalysts for Oxygen Evolution. *Angew. Chem. Int. Ed.* **2019**, *58*, 17458–17464. [CrossRef]
12. Trotochaud, L.; Young, S.L.; Ranney, J.K.; Boettcher, S.W. Nickel-Iron Oxyhydroxide Oxygen-Evolution Electrocatalysts: The Role of Intentional and Incidental Iron Incorporation. *J. Am. Chem. Soc.* **2014**, *136*, 6744–6753. [CrossRef]
13. Klaus, S.; Cai, Y.; Louie, M.W.; Trotochaud, L.; Bell, A.T. Effects of Fe Electrolyte Impurities on Ni(OH)(2)/NiOOH Structure and Oxygen Evolution Activity. *J. Phys. Chem. C* **2015**, *119*, 7243–7254. [CrossRef]
14. Yan, Z.; Sun, H.; Chen, X.; Liu, H.; Zhao, Y.; Li, H.; Xie, W.; Cheng, F.; Chen, J. Anion insertion enhanced electrodeposition of robust metal hydroxide/oxide electrodes for oxygen evolution. *Nat. Commun.* **2018**, *9*, 2373. [CrossRef]
15. Mellsop, S.R.; Gardiner, A.; Johannessen, B.; Marshall, A.T. Structure and transformation of oxy-hydroxide films on Ni anodes below and above the oxygen evolution potential in alkaline electrolytes. *Electrochim. Acta* **2015**, *168*, 356–364. [CrossRef]
16. Bode, H.; Dehmelt, K.; Witte, J. Zur Kenntnis der Nickelhydroxidelektrode. II. Über die Oxydationsprodukte von Nickel(II)-hydroxiden. *Z. Anorg. Allg. Chem.* **1969**, *366*, 1–21. [CrossRef]
17. Cornilsen, B.C.; Shan, X.; Loyselle, P.L. Structural comparison of nickel electrodes and precursor phases. *J. Power Sources* **1990**, *29*, 453–466. [CrossRef]
18. Huang, B.; Xu, H.Y.; Jiang, N.N.; Wang, M.H.; Huang, J.R.; Guan, L.H. Tensile-Strained RuO_2 Loaded on Antimony-Tin Oxide by Fast Quenching for Proton-Exchange Membrane Water Electrolyzer. *Adv. Sci.* **2022**, *9*, 2201654. [CrossRef]
19. Zhang, H.J.; Gao, Y.X.; Xu, H.Y.; Guan, D.Q.; Hu, Z.W.; Jing, C.; Sha, Y.C.; Gu, Y.X.; Huang, Y.C.; Chang, Y.C.; et al. Combined Corner-Sharing and Edge-Sharing Networks in Hybrid Nanocomposite with Unusual Lattice-Oxygen Activation for Efficient Water Oxidation. *Adv. Funct. Mater.* **2022**, *32*, 07618. [CrossRef]
20. Guan, D.; Sh, C.; Xu, H.; Gu, Y.; Zhong, J.; Sha, Y.; Hu, Z.; Ni, M.; Shao, Z. Simultaneously mastering operando strain and reconstruction effects via phase-segregation strategy for enhanced oxygen-evolving electrocatalysis. *J. Energy Chem.* **2023**, *82*, 572–580. [CrossRef]
21. Ding, K.; Zhang, X.; Li, J.P.; Yang, P.; Cheng, X. Phase and morphology evolution of ultrathin $Co(OH)_2$ nanosheets towards supercapacitor application. *Crystengcomm* **2017**, *19*, 5780–5786. [CrossRef]
22. Darbandi, M.; Shaabani, B.; Alizadeh, A.; Yardani, P.; Shahryari, E.; Hosseini, M.G. Preparation and characterization of hexagonal mesoporous beta-$Co(OH)_2$ nanorings. *Micropor. Mesopor. Mat.* **2019**, *284*, 421–426. [CrossRef]

23. Barde, F.; Palacin, M.R.; Beaudoin, B.; Delahaye-Vidal, A.; Tarascon, J.M. New approaches for synthesizing gamma III-CoOOH by soft chemistry. *Chem. Mater.* **2004**, *16*, 299–306. [CrossRef]
24. Dionigi, F.; Zhu, J.; Zheng, Z.; Merzdorf, T.; Sarodnik, H.; Gliech, M.; Pan, L.; Li, W.X.; Greeley, J.; Strasser, P. Intrinsic Electrocatalytic Activity for Oxygen Evolution of Crystalline 3d-Transition Metal Layered Double Hydroxides. *Angew. Chem. Int. Ed.* **2021**, *60*, 14446–14457. [CrossRef] [PubMed]
25. Watanabe, K.I.; Koseki, M.; Kumagai, N. Effect of cobalt addition to nickel hydroxide as a positive material for rechargeable alkaline batteries. *J. Power Sources* **1996**, *58*, 23–28. [CrossRef]
26. Delmas, C.; Tessier, C. Stacking faults in the structure of nickel hydroxide: A rationale of its high electrochemical activity. *J. Mater. Chem.* **1997**, *7*, 1439–1443. [CrossRef]
27. Huang, J.C.; Lei, T.; Wei, X.P.; Liu, X.W.; Liu, T.; Cao, D.X.; Yin, J.L.; Wang, G.L. Effect of Al-doped beta-Ni$(OH)_2$ nanosheets on electrochemical behaviors for high performance supercapacitor application. *J. Power Sources* **2013**, *232*, 370–375. [CrossRef]
28. Jayashree, R.S.; Kamath, P.V. Suppression of the alpha -> beta-nickel hydroxide transformation in concentrated alkali: Role of dissolved cations. *J. Appl. Electrochem.* **2001**, *31*, 1315–1320. [CrossRef]
29. Kamath, P.V.; Dixit, M.; Indira, L.; Shukla, A.K.; Kumar, V.G.; Munichandraiah, N. Stabilized α-Ni$(OH)_2$ as Electrode Material for Alkaline Secondary Cells. *J. Electrochem. Soc.* **1994**, *141*, 2956–2959. [CrossRef]
30. Zhao, Y.L.; Wang, J.M.; Chen, H.; Pan, T.; Zhang, J.Q.; Cao, C.N. Different additives-substituted alpha-nickel hydroxide prepared by urea decomposition. *Electrochim. Acta* **2004**, *50*, 91–98. [CrossRef]
31. Demourgues-Guerlou, L.; Delmas, C. Structure and properties of precipitated nickel-iron hydroxides. *J. Power Sources* **1993**, *45*, 281–289. [CrossRef]
32. Liu, C.J.; Huang, L.H.; Li, Y.W.; Sun, D. Synthesis and electrochemical performance of amorphous nickel hydroxide codoped with Fe^{3+} and $CO_3{}^{2-}$. *Ionics* **2010**, *16*, 215–219. [CrossRef]
33. Zhou, F.; Zhao, X.M.; van Bommel, A.; Rowe, A.W.; Dahn, J.R. Coprecipitation Synthesis of NixMn1-x(OH)(2) Mixed Hydroxides. *Chem. Mater.* **2010**, *22*, 1015–1021. [CrossRef]
34. Luan, C.; Corva, M.; Hagemann, U.; Wang, H.; Heidelmann, M.; Tschulik, K.; Li, T. Atomic-Scale Insights into Morphological, Structural, and Compositional Evolution of CoOOH during Oxygen Evolution Reaction. *ACS Catal.* **2023**, *13*, 1400–1411. [CrossRef]
35. Bott-Neto, J.L.; Rodrigues, M.V.F.; Silva, M.C.; Carneiro-Neto, E.B.; Wosiak, G.; Mauricio, J.C.; Pereira, E.C.; Figueroa, S.J.A.; Fernandez, P.S. Versatile Spectroelectrochemical Cell for In Situ Experiments: Development, Applications, and Electrochemical Behavior. *Chemelectrochem* **2020**, *7*, 4306–4313. [CrossRef]
36. Trzesniewski, B.J.; Diaz-Morales, O.; Vermaas, D.A.; Longo, A.; Bras, W.; Koper, M.T.M.; Smith, W.A. In Situ Observation of Active Oxygen Species in Fe-Containing Ni-Based Oxygen Evolution Catalysts: The Effect of pH on Electrochemical Activity. *J. Am. Chem. Soc* **2015**, *137*, 15112–15121. [CrossRef]
37. Tang, F.; Liu, T.; Jiang, W.L.; Gan, L. Windowless thin layer electrochemical Raman spectroscopy of Ni-Fe oxide electrocatalysts during oxygen evolution reaction. *J. Electroanal. Chem.* **2020**, *871*, 114282. [CrossRef]
38. Nazri, G.; Corrigan, D.A.; Maheswari, S.P. Angle-resolved infrared spectroelectrochemistry. 1. An in situ study of thin-film nickel oxide electrodes. *Langmuir* **1989**, *5*, 17–22. [CrossRef]
39. Drevon, D.; Gorlin, M.; Chernev, P.; Xi, L.F.; Dau, H.; Lange, K.M. Uncovering The Role of Oxygen in Ni-Fe(O_xH_y) Electrocatalysts using In situ Soft X-ray Absorption Spectroscopy during the Oxygen Evolution Reaction. *Sci. Rep.* **2019**, *9*, 1532. [CrossRef]
40. Chen, J.Y.C.; Dang, L.N.; Liang, H.F.; Bi, W.L.; Gerken, J.B.; Jin, S.; Alp, E.E.; Stahl, S.S. Operando Analysis of NiFe and Fe Oxyhydroxide Electrocatalysts for Water Oxidation: Detection of Fe4+ by Mossbauer Spectroscopy. *J. Am. Chem. Soc.* **2015**, *137*, 15090–15093. [CrossRef]
41. Zaharieva, I.; Gonzalez-Flores, D.; Asfari, B.; Pasquini, C.; Mohammadi, M.R.; Klingan, K.; Zizak, I.; Loos, S.; Chernev, P.; Dau, H. Water oxidation catalysis—Role of redox and structural dynamics in biological photosynthesis and inorganic manganese oxides. *Energy Environ. Sci.* **2016**, *9*, 2433–2443. [CrossRef]
42. Smith, R.D.L.; Pasquini, C.; Loos, S.; Chernev, P.; Klingan, K.; Kubella, P.; Mohammadi, M.R.; Gonzalez-Flores, D.; Dau, H. Spectroscopic identification of active sites for the oxygen evolution reaction on iron-cobalt oxides. *Nat. Commun.* **2017**, *8*, 2022. [CrossRef] [PubMed]
43. Francas, L.; Corby, S.; Selim, S.; Lee, D.; Mesa, C.A.; Godin, R.; Pastor, E.; Stephens, I.E.L.; Choi, K.-S.; Durrant, J.R. Spectroelectrochemical study of water oxidation on nickel and iron oxyhydroxide electrocatalysts. *Nat. Commun.* **2019**, *10*, 5208. [CrossRef] [PubMed]
44. Hahn, F.; Floner, D.; Beden, B.; Lamy, C. In situ investigation of the behaviour of a nickel electrode in alkaline solution by UV-Vis and IR reflectance spectroscopies. *Electrochim. Acta* **1987**, *32*, 1631–1636. [CrossRef]
45. Corrigan, D.A.; Knight, S.L. Electrochemical and Spectroscopic Evidence on the Participation of Quadrivalent Nickel in the Nickel Hydroxide Redox Reaction. *J. Electrochem. Soc.* **1989**, *136*, 613–619. [CrossRef]
46. Liu, Q.; Chen, Q.; Zhang, Q.; Xiao, Y.; Zhong, X.; Dong, G.; Delplancke-Ogletree, M.-P.; Terryn, H.; Baert, K.; Reniers, F.; et al. In situ electrochromic efficiency of a nickel oxide thin film: Origin of electrochemical process and electrochromic degradation. *J. Mater. Chem. C* **2018**, *6*, 646–653. [CrossRef]
47. Sahu, D.R.; Wu, T.-J.; Wang, S.-C.; Huang, J.-L. Electrochromic behavior of NiO film prepared by e-beam evaporation. *J. Sci.-Adv. Mater. Dev.* **2017**, *2*, 225–232. [CrossRef]

48. Yuan, Y.; Guo, Y.; Wu, W.; Mao, Z.; Xu, H.; Ma, Y. Kinetics of Active Oxide Species Derived from a Metallic Nickel Surface for Efficient Electrocatalytic Water Oxidation. *ACS Energy Lett.* **2022**, *7*, 3276–3285. [CrossRef]
49. Wu, Y.; Zhao, M.J.; Li, F.; Xie, J.; Li, Y.; He, J.B. Trace Fe Incorporation into Ni-(oxy)hydroxide Stabilizes Ni^{3+} Sites for Anodic Oxygen Evolution: A Double Thin-Layer Study. *Langmuir* **2020**, *36*, 5126–5133. [CrossRef]
50. Bendert, R.M.; Corrigan, D.A. Effect of Coprecipitated Metal Ions on the Electrochromic Properties of Nickel Hydroxide. *J. Electrochem. Soc.* **1989**, *136*, 1369–1374. [CrossRef]
51. Gorlin, M.; de Araujo, J.F.; Schmies, H.; Bernsmeier, D.; Dresp, S.; Gliech, M.; Jusys, Z.; Chernev, P.; Kraehnert, R.; Dau, H.; et al. Tracking Catalyst Redox States and Reaction Dynamics in Ni-Fe Oxyhydroxide Oxygen Evolution Reaction Electrocatalysts: The Role of Catalyst Support and Electrolyte pH. *J. Am. Chem. Soc.* **2017**, *139*, 2070–2082. [CrossRef]
52. Loos, S.; Zaharieva, I.; Chernev, P.; Lissner, A.; Dau, H. Electromodified NiFe Alloys as Electrocatalysts for Water Oxidation: Mechanistic Implications of Time-Resolved UV/Vis Tracking of Oxidation State Changes. *Chemsuschem* **2019**, *12*, 1966–1976. [CrossRef]
53. Burke, M.S.; Zou, S.H.; Enman, L.J.; Kellon, J.E.; Gabor, C.A.; Pledger, E.; Boettcher, S.W. Revised Oxygen Evolution Reaction Activity Trends for First-Row Transition-Metal (Oxy)hydroxides in Alkaline Media. *J. Phys. Chem. Lett.* **2015**, *6*, 3737–3742. [CrossRef]
54. Smith, R.D.L.; Pasquini, C.; Loos, S.; Chernev, P.; Klingan, K.; Kubella, P.; Mohammadi, M.R.; Gonzalez-Flores, D.; Dau, H. Geometric distortions in nickel (oxy)hydroxide electrocatalysts by redox inactive iron ions. *Energy Environ. Sci.* **2018**, *11*, 2476–2485. [CrossRef]
55. Goldsmith, Z.K.; Harshan, A.K.; Gerken, J.B.; Voros, M.; Galli, G.; Stahl, S.S.; Hammes-Schiffer, S. Characterization of NiFe oxyhydroxide electrocatalysts by integrated electronic structure calculations and spectroelectrochemistry. *Proc. Natl. Acad. Sci. USA* **2017**, *114*, 3050–3055. [CrossRef]
56. Louie, M.W.; Bell, A.T. An Investigation of Thin-Film Ni-Fe Oxide Catalysts for the Electrochemical Evolution of Oxygen. *J. Am. Chem. Soc.* **2013**, *135*, 12329–12337. [CrossRef]
57. Gao, P.; Gosztola, D.; Leung, L.-W.H.; Weaver, M.J. Surface-enhanced Raman scattering at gold electrodes: Dependence on electrochemical pretreatment conditions and comparisons with silver. *J. Electroanal. Chem. Interf. Electrochem.* **1987**, *233*, 211–222. [CrossRef]
58. Desilvestro, J.; Weaver, M.J. Surface structural changes during oxidation of gold electrodes in aqueous media as detected using surface-enhanced Raman spectroscopy. *J. Electroanal. Chem. Interf. Electrochem.* **1986**, *209*, 377–386. [CrossRef]
59. Yeo, B.S.; Bell, A.T. In Situ Raman Study of Nickel Oxide and Gold-Supported Nickel Oxide Catalysts for the Electrochemical Evolution of Oxygen. *J. Phys. Chem. C* **2012**, *116*, 8394–8400. [CrossRef]
60. Kostecki, R.; McLarnon, F. Electrochemical and in situ Raman spectroscopic characterization of nickel hydroxide electrodes. *J. Electrochem. Soc.* **1997**, *144*, 485–493. [CrossRef]
61. Merrill, M.; Worsley, M.; Wittstock, A.; Biener, J.; Stadermann, M. Determination of the "NiOOH" charge and discharge mechanisms at ideal activity. *J. Electroanal. Chem.* **2014**, *717*, 177–188. [CrossRef]
62. Diaz-Morales, O.; Ferrus-Suspedra, D.; Koper, M.T.M. The importance of nickel oxyhydroxide deprotonation on its activity towards electrochemical water oxidation. *Chem. Sci.* **2016**, *7*, 2639–2645. [CrossRef] [PubMed]
63. Lo, Y.L.; Hwang, B.J. In situ Raman studies on cathodically deposited nickel hydroxide films and electroless Ni-P electrodes in 1 M KOH solution. *Langmuir* **1998**, *14*, 944–950. [CrossRef]
64. Chen, D.C.; Xiong, X.H.; Zhao, B.T.; Mahmoud, M.A.; El-Sayed, M.A.; Liu, M.L. Probing Structural Evolution and Charge Storage Mechanism of NiO_2H_x Electrode Materials using In Operando Resonance Raman Spectroscopy. *Adv. Sci.* **2016**, *3*, 1500433. [CrossRef] [PubMed]
65. Moysiadou, A.; Lee, S.; Hsu, C.-S.; Chen, H.M.; Hu, X. Mechanism of Oxygen Evolution Catalyzed by Cobalt Oxyhydroxide: Cobalt Superoxide Species as a Key Intermediate and Dioxygen Release as a Rate-Determining Step. *J. Am. Chem. Soc.* **2020**, *142*, 11901–11914. [CrossRef]
66. Yeo, B.S.; Bell, A.T. Enhanced Activity of Gold-Supported Cobalt Oxide for the Electrochemical Evolution of Oxygen. *J. Am. Chem. Soc.* **2011**, *133*, 5587–5593. [CrossRef]
67. Ye, S.; Wang, J.; Hu, J.; Chen, Z.; Zheng, L.; Fu, Y.; Lei, Y.; Ren, X.; He, C.; Zhang, Q.; et al. Electrochemical Construction of Low-Crystalline CoOOH Nanosheets with Short-Range Ordered Grains to Improve Oxygen Evolution Activity. *ACS Catal.* **2021**, *11*, 6104–6112. [CrossRef]
68. De Faria, D.L.A.; Silva, S.V.; de Oliveira, M.T. Raman microspectroscopy of some iron oxides and oxyhydroxides. *J. Raman Spectrosc.* **1997**, *28*, 873–878. [CrossRef]
69. Steimecke, M.; Seiffarth, G.; Bron, M. In Situ Characterization of Ni and Ni/Fe Thin Film Electrodes for Oxygen Evolution in Alkaline Media by a Raman-Coupled Scanning Electrochemical Microscope Setup. *Anal. Chem.* **2017**, *89*, 10679–10686. [CrossRef]
70. Lee, S.; Bai, L.C.; Hu, X.L. Deciphering Iron-Dependent Activity in Oxygen Evolution Catalyzed by Nickel-Iron Layered Double Hydroxide. *Angew. Chem. Int. Ed.* **2020**, *59*, 8072–8077. [CrossRef]
71. Lee, S.; Banjac, K.; Lingenfelder, M.; Hu, X. Oxygen Isotope Labeling Experiments Reveal Different Reaction Sites for the Oxygen Evolution Reaction on Nickel and Nickel Iron Oxides. *Angew. Chem. Int. Ed.* **2019**, *58*, 10295–10299. [CrossRef]
72. Bo, X.; Li, Y.B.; Chen, X.J.; Zhao, C. Operando Raman Spectroscopy Reveals Cr-Induced-Phase Reconstruction of NiFe and CoFe Oxyhydroxides for Enhanced Electrocatalytic Water Oxidation. *Chem. Mater.* **2020**, *32*, 4303–4311. [CrossRef]

73. Sagui, N.A.; Strom, P.; Edvinsson, T.; Pehlivan, I.B. Nickel Site Modification by High-Valence Doping: Effect of TantalumImpurities on the Alkaline Water Electro-Oxidation by NiO Probedby Operando Raman Spectroscopy. *ACS Catal.* **2022**, *12*, 6506–6516. [CrossRef]
74. Hall, D.S.; Lockwood, D.J.; Poirier, S.; Bock, C.; MacDougall, B.R. Applications of in Situ Raman Spectroscopy for Identifying Nickel Hydroxide Materials and Surface Layers during Chemical Aging. *ACS Appl. Mater. Inter.* **2014**, *6*, 3141–3149. [CrossRef]
75. Qiu, Z.; Tai, C.-W.; Niklasson, G.A.; Edvinsson, T. Direct observation of active catalyst surface phases and the effect of dynamic self-optimization in NiFe-layered double hydroxides for alkaline water splitting. *Energy Environ. Sci.* **2019**, *12*, 572–581. [CrossRef]
76. Desilvestro, J.; Corrigan, D.A.; Weaver, M.J. Spectroelectrochemistry of thin nickel hydroxide films on gold using surface-enhanced Raman spectroscopy. *J. Phys. Chem.* **1986**, *90*, 6408–6411. [CrossRef]
77. Yu, P.C.; Lampert, C.M. In-situ spectroscopic studies of electrochromic hydrated nickel-oxide films. *Sol. Energy Mater.* **1989**, *19*, 1–16. [CrossRef]
78. Zhang, M.; Frei, H. Water Oxidation Mechanisms of Metal Oxide Catalysts by Vibrational Spectroscopy of Transient Intermediates. *Annu. Rev. Phys. Chem.* **2017**, *68*, 209–231. [CrossRef]
79. Mansour, A.N.; Melendres, C.A. Analysis of X-ray absorption spectra of some nickel oxycompounds using theoretical standards. *J. Phys. Chem. A* **1998**, *102*, 65–81. [CrossRef]
80. Goerlin, M.; Chernev, P.; de Araujo, J.F.; Reier, T.; Dresp, S.; Paul, B.; Kraehnert, R.; Dau, H.; Strasser, P. Oxygen Evolution Reaction Dynamics, Faradaic Charge Efficiency, and the Active Metal Redox States of Ni-Fe Oxide Water Splitting Electrocatalysts. *J. Am. Chem. Soc.* **2016**, *138*, 5603–5614. [CrossRef]
81. Friebel, D.; Louie, M.W.; Bajdich, M.; Sanwald, K.E.; Cai, Y.; Wise, A.M.; Cheng, M.J.; Sokaras, D.; Weng, T.C.; Alonso-Mori, R.; et al. Identification of Highly Active Fe Sites in (Ni,Fe)OOH for Electrocatalytic Water Splitting. *J. Am. Chem. Soc.* **2015**, *137*, 1305–1313. [CrossRef]
82. Gonzalez-Flores, D.; Klingan, K.; Chernev, P.; Loos, S.; Mohammadi, M.R.; Pasquini, C.; Kubella, P.; Zaharieva, I.; Smith, R.D.L.; Dau, H. Nickel-iron catalysts for electrochemical water oxidation—Redox synergism investigated by in situ X-ray spectroscopy with millisecond time resolution. *Sustain. Energy Fuels* **2018**, *2*, 1986–1994. [CrossRef]
83. Abbott, D.F.; Fabbri, E.; Borlaf, M.; Bozza, F.; Schaublin, R.; Nachtegaal, M.; Graule, T.; Schmidt, T.J. Operando X-ray absorption investigations into the role of Fe in the electrochemical stability and oxygen evolution activity of $Ni_{1-x}Fe_xO_y$ nanoparticles. *J. Mater. Chem. A* **2018**, *6*, 24534–24549. [CrossRef]
84. Trzesniowski, H.; Deka, N.; van der Heijden, O.; Golnak, R.; Xiao, J.; Koper, M.T.M.; Seidel, R.; Mom, R.V. Reversible and Irreversible Cation Intercalation in NiFeOX Oxygen Evolution Catalysts in Alkaline Media. *J. Phys. Chem. Lett.* **2023**, *14*, 545–551. [CrossRef] [PubMed]
85. Kuai, C.; Zhang, Y.; Wu, D.; Sokaras, D.; Mu, L.; Spence, S.; Nordlund, D.; Lin, F.; Du, X.-W. Fully Oxidized Ni-Fe Layered Double Hydroxide with 100% Exposed Active Sites for Catalyzing Oxygen Evolution Reaction. *ACS Catal.* **2019**, *9*, 6027–6032. [CrossRef]
86. Yu, H.M.; Yang, X.; Xiao, X.; Chen, M.; Zhang, Q.H.; Huang, L.; Wu, J.B.; Li, T.Q.; Chen, S.M.; Song, L.; et al. Atmospheric-Pressure Synthesis of 2D Nitrogen-Rich Tungsten Nitride. *Adv. Mater.* **2018**, *30*, 05655. [CrossRef]
87. Kuai, C.; Xu, Z.; Xi, C.; Hu, A.; Yang, Z.; Zhang, Y.; Sun, C.-J.; Li, L.; Sokaras, D.; Dong, C.; et al. Phase segregation reversibility in mixed-metal hydroxide water oxidation catalysts. *Nat. Catal.* **2020**, *3*, 743–753. [CrossRef]
88. Enman, L.J.; Stevens, M.B.; Dahan, M.H.; Nellist, M.R.; Toroker, M.C.; Boettcher, S.W. Operando X-Ray Absorption Spectroscopy Shows Iron Oxidation Is Concurrent with Oxygen Evolution in Cobalt-Iron (Oxy)hydroxide Electrocatalysts. *Angew. Chem. Int. Ed.* **2018**, *57*, 12840–12844. [CrossRef]
89. Pasquini, C.; Zaharieva, I.; Gonzalez-Flores, D.; Chernev, P.; Mohammadi, M.R.; Guidoni, L.; Smith, R.D.L.; Dau, H. H/D Isotope Effects Reveal Factors Controlling Catalytic Activity in Co-Based Oxides for Water Oxidation. *J. Am. Chem. Soc.* **2019**, *141*, 2938–2948. [CrossRef]
90. Risch, M.; Klingan, K.; Heidkamp, J.; Ehrenberg, D.; Chernev, P.; Zaharieva, I.; Dau, H. Nickel-oxido structure of a water-oxidizing catalyst film. *Chem. Commun.* **2011**, *47*, 11912–11914. [CrossRef]
91. Risch, M.; Khare, V.; Zaharieva, I.; Gerencser, L.; Chernev, P.; Dau, H. Cobalt-Oxo Core of a Water-Oxidizing Catalyst Film. *J. Am. Chem. Soc.* **2009**, *131*, 6936. [CrossRef]
92. Niemantsverdriet, J.W.; Delgass, W.N. In situ Mossbauer spectroscopy in catalysis. *Top. Catal.* **1999**, *8*, 133–140. [CrossRef]
93. Kasian, O.; Geiger, S.; Mayrhofer, K.J.J.; Cherevko, S. Electrochemical On-line ICP-MS in Electrocatalysis Research. *Chem. Rec.* **2019**, *19*, 2130–2142. [CrossRef]
94. Kasian, O.; Geiger, S.; Li, T.; Grote, J.P.; Schweinar, K.; Zhang, S.Y.; Scheu, C.; Raabe, D.; Cherevko, S.; Gault, B.; et al. Degradation of iridium oxides via oxygen evolution from the lattice: Correlating atomic scale structure with reaction mechanisms. *Energy Environ. Sci.* **2019**, *12*, 3548–3555. [CrossRef]
95. Kasian, O.; Geiger, S.; Stock, P.; Polymeros, G.; Breitbach, B.; Savan, A.; Ludwig, A.; Cherevko, S.; Mayrhofer, K.J.J. On the Origin of the Improved Ruthenium Stability in RuO_2-IrO_2 Mixed Oxides. *J. Electrochem. Soc.* **2016**, *163*, F3099–F3104. [CrossRef]
96. Ko, Y.J.; Han, M.H.; Kim, H.; Kim, J.Y.; Lee, W.H.; Kim, J.; Kwak, J.Y.; Kim, C.H.; Park, T.E.; Yu, S.H.; et al. Unraveling Ni-Fe 2D nanostructure with enhanced oxygen evolution via in situ and operando spectroscopies. *Chem Catal.* **2022**, *2*, 2312–2327. [CrossRef]

97. Oliver-Tolentino, M.A.; Vazquez-Samperio, J.; Manzo-Robledo, A.; Gonzalez-Huerta, R.D.; Flores-Moreno, J.L.; Ramirez-Rosales, D.; Guzman-Vargas, A. An Approach to Understanding the Electrocatalytic Activity Enhancement by Superexchange Interaction toward OER in Alkaline Media of Ni-Fe LDH. *J. Phys. Chem. C* **2014**, *118*, 22432–22438. [CrossRef]
98. Dionigi, F.; Zeng, Z.H.; Sinev, I.; Merzdorf, T.; Deshpande, S.; Lopez, M.B.; Kunze, S.; Zegkinoglou, I.; Sarodnik, H.; Fan, D.X.; et al. In-situ structure and catalytic mechanism of NiFe and CoFe layered double hydroxides during oxygen evolution. *Nat. Commun.* **2020**, *11*, 2522. [CrossRef]
99. Roy, C.; Sebok, B.; Scott, S.B.; Fiordaliso, E.M.; Sorensen, J.E.; Bodin, A.; Trimarco, D.B.; Damsgaard, C.D.; Vesborg, P.C.K.; Hansen, O.; et al. Impact of nanoparticle size and lattice oxygen on water oxidation on NiFeOxHy. *Nat. Catal.* **2018**, *1*, 820–829. [CrossRef]
100. De Araujo, J.F.; Dionigi, F.; Merzdorf, T.; Oh, H.S.; Strasser, P. Evidence of Mars-Van-Krevelen Mechanism in the Electrochemical Oxygen Evolution on Ni-Based Catalysts. *Angew. Chem. Int. Ed.* **2021**, *60*, 14981–14988. [CrossRef]
101. Bard, A.J.; Fan, F.R.F.; Kwak, J.; Lev, O. Scanning Electrochemical Microscopy—Introduction and Principles. *Anal. Chem.* **1989**, *61*, 132–138. [CrossRef]
102. Kai, T.H.; Zoski, C.G.; Bard, A.J. Scanning electrochemical microscopy at the nanometer level. *Chem. Commun.* **2018**, *54*, 1934–1947. [CrossRef] [PubMed]
103. Ahn, H.S.; Bard, A.J. Surface Interrogation Scanning Electrochemical Microscopy of $Ni_{1-x}Fe_xOOH$ ($0 < x < 0.27$) Oxygen Evolving Catalyst: Kinetics of the "fast" Iron Sites. *J. Am. Chem. Soc.* **2016**, *138*, 313–318. [CrossRef] [PubMed]
104. Rodriguez-Lopez, J.; Alpuche-Aviles, M.A.; Bard, A.J. Interrogation of Surfaces for the Quantification of Adsorbed Species on Electrodes: Oxygen on Gold and Platinum in Neutral Media. *J. Am. Chem. Soc.* **2008**, *130*, 16985–16995. [CrossRef]
105. Ahn, H.S.; Bard, A.J. Surface Interrogation of CoPi Water Oxidation Catalyst by Scanning Electrochemical Microscopy. *J. Am. Chem. Soc.* **2015**, *137*, 612–615. [CrossRef]
106. Wehrens-Dijksma, M.; Notten, P.H.L. Electrochemical Quartz Microbalance characterization of $Ni(OH)_2$-based thin film electrodes. *Electrochim. Acta* **2006**, *51*, 3609–3621. [CrossRef]